Materials Today Advances 7 (2020) 100078

Contents lists available at ScienceDirect

Materials Today Advances

journal homepage: www.journals.elsevier.com/materials-today-advances/

Recent advances in cathode materials of rechargeable aqueous zinc-ion batteries

L. Wang, J. Zheng*

College of Chemistry and Molecular Engineering, Beijing National Laboratory for Molecular Sciences, Peking University, Beijing 100871, China

ARTICLE INFO

Article history:
Received 26 March 2020
Received in revised form
25 April 2020
Accepted 1 May 2020
Available online 23 June 2020

Keywords:
Aqueous zinc-ion battery
Mild aqueous electrolyte
Cathode materials
Energy storage mechanism
Challenges and perspectives

ABSTRACT

Given good safety, low cost, and environmental friendliness, rechargeable aqueous zinc-ion batteries (ZIBs) are considered as a more feasible solution for grid-scale applications than Li-ion batteries. The availability of suitable cathode materials to store Zn^{2+} is a prerequisite to realize high-performance aqueous ZIBs. However, due to the high polarization of bivalent Zn^{2+}, Zn-host cathode materials with excellent electrochemical performances are yet to be discovered. In this review, recent advances in the cathode materials of aqueous ZIBs, including different types of cathode materials, electrode reaction mechanisms, and strategies to enhance their electrochemical performance, are briefed. Finally, current challenges and perspectives on the cathodes of ZIBs are presented.

1. Introduction

The concerns about potential energy crisis and environmental pollution have pushed the search for renewable and low-cost electrochemical energy storage systems to store and make the best use of intermittent and dispersed renewable energy sources such as solar, wind power, and tidal energy [1–3]. Among various energy storage systems, Li-ion batteries with high energy densities and long cycle life dominate commercial rechargeable battery market and are ubiquitous in portable electronics and electric vehicles [4,5]. Nevertheless, their large-scale deployment is plagued by limited lithium resources, environmental impact, and safety hazards arising from flammable organic electrolytes [6,7]. Aqueous batteries have garnered considerable interest and are promising candidates for grid-scale electrochemical energy storage owing to the following unique merits:

(1) Aqueous electrolytes offer several orders of magnitude higher ionic conductivities (≈1 S/cm) than non-aqueous electrolytes (≈10^{-2}–10^{-3} S/cm), favoring high rate capability and high power density [8].
(2) In contrast with the toxicity and flammability of non-aqueous electrolytes, aqueous electrolytes can be non-toxic and non-flammable, minimizing negative environmental impacts and safety hazards.
(3) Compared with non-aqueous batteries assembled in the inert-gas glove box, aqueous batteries can be assembled in air, which greatly eases the manufacturing procedure and reduces the production cost.

To date, a variety of aqueous batteries using naturally abundant alkali metal cations (e.g. Li^+, Na^+, and K^+) [9–11] as well as multivalent cations (e.g. Mg^{2+}, Al^{3+}, and Zn^{2+}) [12–14] as charge carriers have been explored. In comparison with Li- or Na-ion batteries with a single-electron transfer, the systems using multivalent ions (e.g. Mg^{2+}, Al^{3+}, and Zn^{2+}) can achieve higher storage capacity and energy density due to multiple electron transfer involved in redox reactions [15–17]. Although Mg and Al metals offer large gravimetric capacity (Table 1), they cannot be directly used as anode materials in aqueous electrolytes because of anode passivation and incompatible redox potentials, which hinders the transport of Mg^{2+}/Al^{3+} ions and causes cell failure [18,19]. In addition, the available electrode materials as insertion host for Mg^{2+}/Al^{3+} ions are limited owing to the sluggish Mg^{2+}/Al^{3+} ion diffusion in host lattices, which largely restricts the development of aqueous Mg/Al–ion battery [12,20,21].

* Corresponding author.
E-mail address: junrong@pku.edu.cn (J. Zheng).

https://doi.org/10.1016/j.mtadv.2020.100078

Table 1
A comparison of the characteristics of Zn^{2+} ions with other available charge carrier ions being explored for rechargeable aqueous batteries.

Element	Li^+	Na^+	K^+	Mg^{2+}	Zn^{2+}	Al^{3+}
Ionic radius (Å) [41]	0.76	1.02	1.38	0.72	0.74	0.535
Hydrated ionic radius (Å) [42]	3.82	3.58	3.31	4.28	4.30	4.75
Relative atomic mass (g/mol)	6.94	23.00	39.10	24.31	65.38	26.98
Standard potential (V vs. SHE) [43]	−3.04	−2.71	−2.93	−2.37	−0.76	−1.66
Theoretical specific capacity (mAh/g)	3,862	1,166	685	2,205	820	2,980
Specific volumetric capacity (mAh/cm^3)	2,061	1,129	610	3,834	5,851	8,046
Crustal abundance (ppm)	20	23,550	20,850	23,300	79	82,300

In this regard, rechargeable zinc-ion batteries (ZIBs) based on Zn^{2+} intercalation chemistry hold overwhelming advantages over others because of the utilization of Zn metal anode. Table 1 shows a comparison of the characteristics of Zn^{2+} ions with other available charge carrier ions. The properties of Zn anodes include the following: low cost arising from high abundance and large-scale production; non-toxicity; high theoretical capacity (820 mAh/g) [15,22]; relatively low redox potential (−0.76 V vs. standard hydrogen electrode [SHE]) [23], and impressive electrochemical stability in water because of a high overpotential for hydrogen evolution [22]. In 1986, Yamamoto and Shoji [24] designed a rechargeable aqueous Zn−MnO_2 battery with mild neutral $ZnSO_4$ aqueous electrolyte. The introduction of mild neutral electrolyte into the ZIBs addresses the issues of environmental concerns and the formation of irreversible byproducts (ZnO, $Zn(OH)_2$, etc.), which are prevalent in alkaline zinc cells [25]. With the feasible electrolyte and anode, the discharge capacity and energy density of ZIBs mainly depend on the cathode materials. Thus, seeking suitable cathode materials is crucial to the development of aqueous ZIBs. Despite the relative small ionic radius of Zn^{2+} ions (0.74 Å) and the shield effect of co-insertion of water molecules, the large atomic mass and the strong electrostatic interaction between Zn^{2+} ions and crystal structures of cathode caused by the high charge density of divalent Zn^{2+} ions result in sluggish transport kinetics and diffusion process in a bulk electrode [26]. Therefore, it is a very challenging task to find suitable cathodes with superior electrochemical performances. The development of the cathode materials as the insertion hosts of Zn^{2+} ions is still at the infancy stage. To date, four main categories including Prussian blue analogs (PBAs) [27−30], manganese oxides [8,26,31], vanadium-based compounds [32−34], and organics have been reported as cathodes for ZIBs. The related reaction mechanisms are complicated and underdeveloped, which are subject to crystallographic structures, composition and morphology of cathode materials, and exert a great effect on the electrochemical performances of aqueous ZIBs [35]. PBAs deliver limited specific capacities with high working voltage [29,30], while vanadium-based compounds exhibit high capacities with low operating voltage, high rate capability, and stable cyclability [8,36−38]. In contrast, manganese oxides and organics have relatively high specific capacities and working voltages [26,31,39,40]. The four kinds of cathode materials possess respective advantages and disadvantages, and none of them has satisfactory comprehensive performances in terms of energy density, rate capability, and cycling stability. They suffer from structural failure, sluggish diffusion kinetics, low energy density, and inadequate cycle life. Thus, it remains a great challenge to improve the electrochemical properties of cathode materials, and corresponding optimizing strategies should be proposed and investigated.

In this review, we will summarize recently developed cathode materials and their reaction mechanisms during charge and discharge. Moreover, optimization strategies to improve electrochemical performances of aqueous ZIBs are also proposed. At last, we present emerging challenges and future perspectives of developing cathode materials for aqueous ZIBs, aiming to stimulate more research on ZIBs and promote their practical applications.

2. Electrode reaction mechanisms

Compared to the insertion reaction mechanism in aqueous alkali metal-ion batteries, the energy storage mechanisms for aqueous ZIBs are more complicated and controversial. The following four main reaction mechanisms in aqueous ZIBs have been proposed: the reversible Zn^{2+} insertion/extraction; the chemical conversion reactions; the reversible Zn^{2+} and H^+ co-insertion/extraction, and dissolution−deposition reaction mechanism.

2.1. The Zn^{2+} insertion/extraction mechanism

The reversible Zn^{2+} insertion/extraction reaction is the dominant mechanism of cathode materials in ZIBs. For instance, Kang et al. [23] reported a rechargeable Zn/$ZnSO_4$/α-MnO_2 battery, which operates through the reversible migration of Zn^{2+} ions between the tunnels of α-MnO_2 cathode and Zn anode (Fig. 1a). X-ray diffraction (XRD) patterns of α-MnO_2 electrode at the discharge state (Fig. 1b) confirm that the formation of $ZnMn_2O_4$, indicating Zn^{2+} ions insert into α-MnO_2 during discharge. On charging, the electrode recovers to α-MnO_2, suggesting the extraction of Zn^{2+} ions during charge. Thereby, the reaction mechanism of the Zn/α-MnO_2 batteries can be described as follows:

$$\text{Cathode: } 2MnO_2 + Zn^{2+} + 2e^- \leftrightarrow ZnMn_2O_4 \quad (1)$$

$$\text{Anode: } Zn \leftrightarrow Zn^{2+} + 2e^- \quad (2)$$

Other MnO_2 polymorphs (β-, γ-, λ-, and δ-type) [44−47] also operate through Zn-ion intercalation chemistry.

V-based cathode materials have also been validated to enable the insertion/extraction of divalent Zn^{2+} ions. Nazar et al. [8] reported $Zn_{0.25}V_2O_5 \cdot nH_2O$ nanobelts cathode based on reversible Zn^{2+} insertion/extraction mechanism in aqueous ZIBs (Fig. 1c). The cathode delivers a specific capacity of 282 mAh/g at 300 mA/g, corresponding to the insertion/extraction of ~1.1 Zn^{2+} into/from $Zn_{0.25}V_2O_5 \cdot nH_2O$, which can be described as follows:

$$Zn_{0.25}V_2O_5 \cdot nH_2O + 1.1Zn^{2+} + 2.2e^- \leftrightarrow Zn_{1.35}V_2O_5 \cdot nH_2O\,. \quad (3)$$

The operando XRD investigation provides significant insights into the insertion mechanism and dynamic structural evolution in $Zn_xV_2O_5$ during charge/discharge (Fig. 1d). On immersing in the electrolyte, the interlayer distance increases from 10.8 Å to 12.9 Å. For $x < 0.55$ during discharge, an increased screening of the interlayer electrostatic repulsion with increasing Zn^{2+} content results in a small contraction of the interlayer distance. In the $0.55 < x < 0.6$ range, the expulsion of water from the interlayer and an additional effect from intercalated zinc pin the layers together, leading to the sharp interlayer distance contraction from 12.3 Å to 11.0 Å. Then the

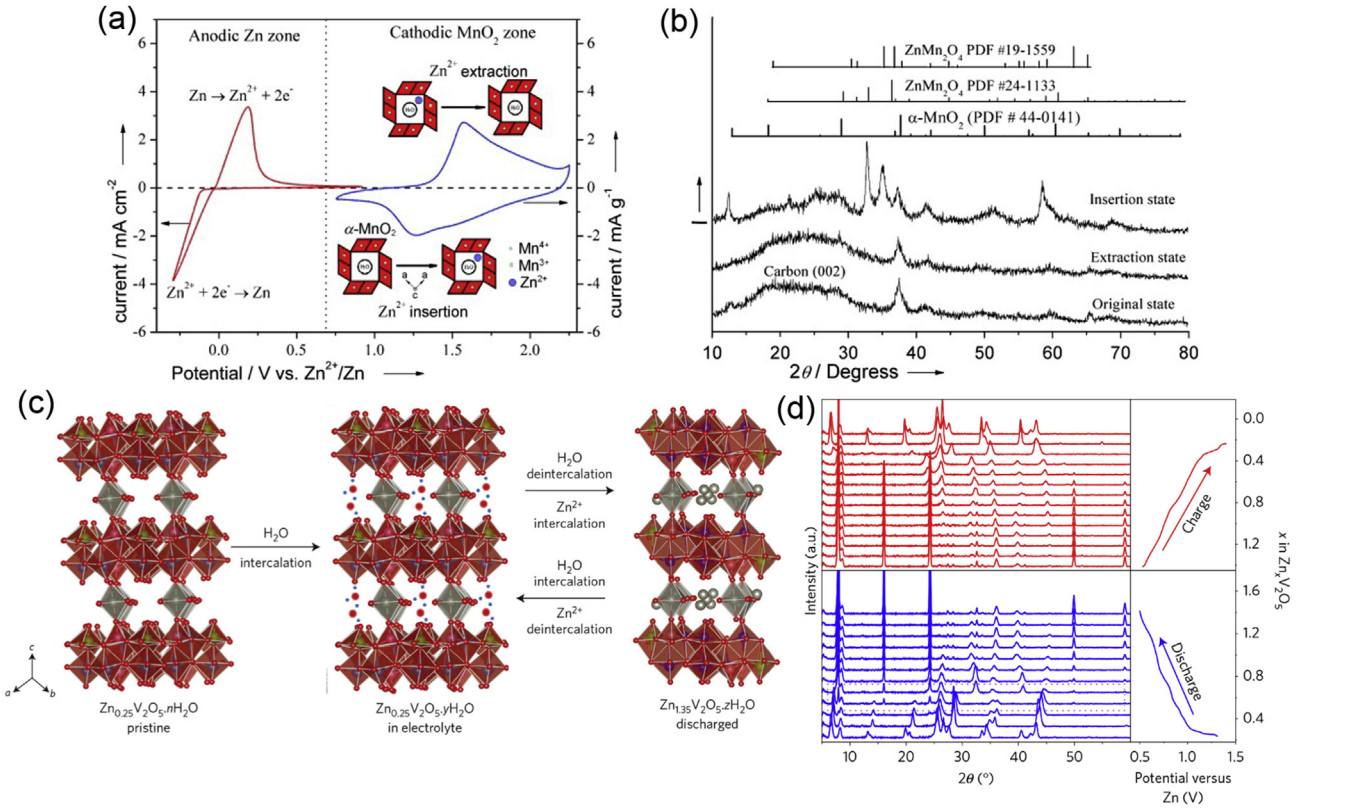

Fig. 1. (a) The reversible Zn^{2+} insertion/extraction mechanism in the α-MnO_2. (b) XRD patterns of cathodic crystalline α-MnO_2 electrodes in the original, extraction, and insertion states [23]. (c) Scheme showing reversible water intercalation into $Zn_{0.25}V_2O_5 \cdot nH_2O$ immersed in electrolyte/H_2O, and the water deintercalation accompanying Zn^{2+} intercalation upon electrochemical discharge. (d) Operando XRD patterns of $Zn_{0.25}V_2O_5 \cdot nH_2O$ during the second electrochemical cycle [8].

new set of (001) reflections show constant position and increased intensity, whereas the intensity and position of other peaks (26°, 32° and 40°) change, indicating that the structure continues to evolve with Zn^{2+} insertion. In the subsequent charge process, the structural evolution follows the reverse trend to that of discharge. The reversible Zn^{2+} insertion/extraction mechanism goes for PBAs and organic cathode materials too, which will be discussed in the next section.

2.2. Chemical conversion reactions

In addition to the conventional Zn^{2+} insertion/extraction mechanism, a chemical conversion reaction has been revealed in a Zn/α-MnO_2 battery system, which operates through the chemical conversion reaction between α-MnO_2 and MnOOH [26]. During discharge, MnO_2 reacts with proton from water to form MnOOH and the resulted OH^- ions react with $ZnSO_4$ and H_2O in the electrolyte to form flake-like $ZnSO_4$ $[Zn(OH)_2]$ xH_2O, reaching a neutral charge state in the system. The morphological and structural evolution of α-MnO_2 cathode during charge/discharge were comprehensively investigated by means of transmission electron microscopy (TEM) and scanning transmission electron microscopy–energy dispersive spectroscopy (STEM–EDS) coupled with XRD. Although XRD signal of consequent products of $ZnSO_4$ $[Zn(OH)_2]_3$ xH_2O dominates the XRD patterns of other phases (Fig. 2a), the lattice distances of 0.33 and 0.26 nm from the discharged nanorods and nanoparticle aggregates match the d spaces from the (210) and (020) planes in monoclinic MnOOH (Fig. 2b&c), indicating the formation of MnOOH. In addition, STEM–EDS mappings reveal that the nanorods and nanoparticles consist of O and Mn elements (Fig. 2d), whereas Zn is mainly distributed in the large flake-like solid (Fig. 2e), further confirming the above conversion reaction. Upon charging, the MnOOH reverts to the original α-MnO_2, and $ZnSO_4$ $[Zn(OH)_2]_3$ xH_2O subsequently decomposes, implying reversible electrochemical reaction between MnO_2 and MnOOH. Thus, the electrochemical reactions of the Zn/α-MnO_2 batteries can be described as follows:

$$\text{Cathode: } MnO_2 + H^+ + e^- \leftrightarrow MnOOH \quad (4)$$

$$1/2\ Zn^{2+} + 1/6ZnSO_4 + OH^- + x/6H_2O \leftrightarrow 1/6ZnSO_4[Zn(OH)_2]_3 \cdot xH_2O \quad (5)$$

$$\text{Anode: } 1/2Zn \leftrightarrow 1/2Zn^{2+} + e^- \quad (6)$$

2.3. Zn^{2+} and H^+ co-insertion/extraction mechanisms

2.3.1. Step-wise Zn^{2+} and H^+ insertion/extraction mechanism

It is reasonable to speculate that H^+ can insert into the cathode material with open framework in mild electrolyte conditions due to the much smaller size of H^+. Wang et al. [31] demonstrated a step-wise H^+ and Zn^{2+} insertion reaction mechanism with a distinct difference in reaction kinetics during discharge in aqueous Zn/ϵ-MnO_2 battery. The charge and discharge curves of the Zn/ϵ-MnO_2 cells can be separated into two distinct reaction regions (Fig. 3a). With increasing charge and discharge rate, the voltage and capacity drops in region I are much smaller than those in region II, demonstrating extremely faster reaction kinetics in region I. The discharge GITT profiles in region II show much bigger overvoltage (0.6 V) than that in region I (0.08 V) (Fig. 3b), which is attributed to

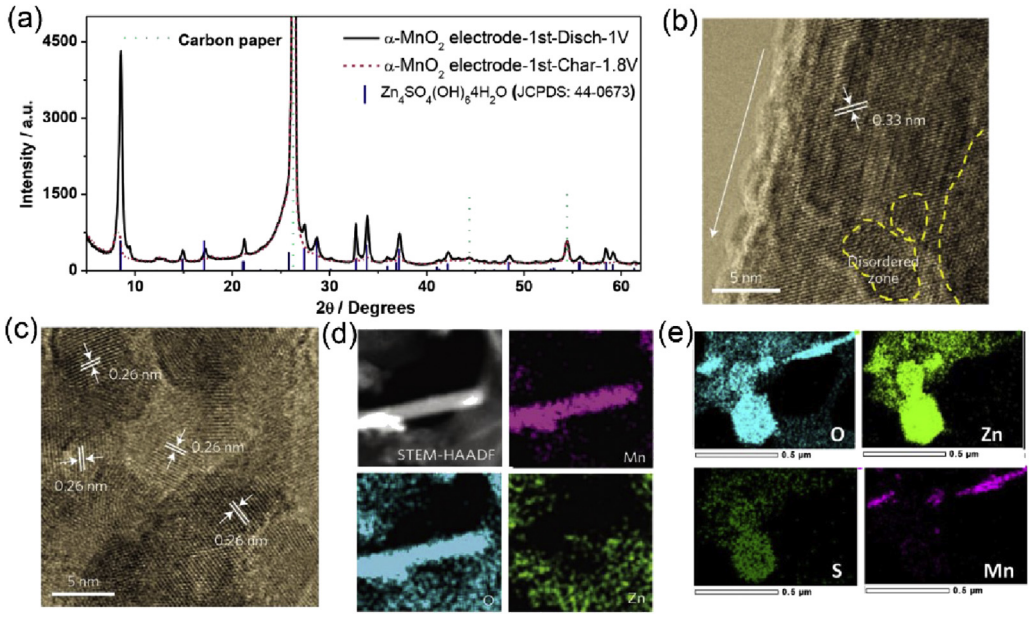

Fig. 2. (a) XRD patterns of α-MnO_2 electrodes discharged to 1 V and charged back to 1.8 V in the first cycle. (b and c) High-resolution transmission electron microscopy images and (d) Scanning transmission electron microscopy–energy dispersive spectroscopy (STEM–EDS) mapping of the elemental distributions of Mn, O, and Zn of the MnO_2 electrodes discharged to 1 V in the first cycle. (e) STEM–EDS mappings for elements of O, Zn, S, and Mn in α-MnO_2 electrodes discharged to 1 V in the first cycle [26].

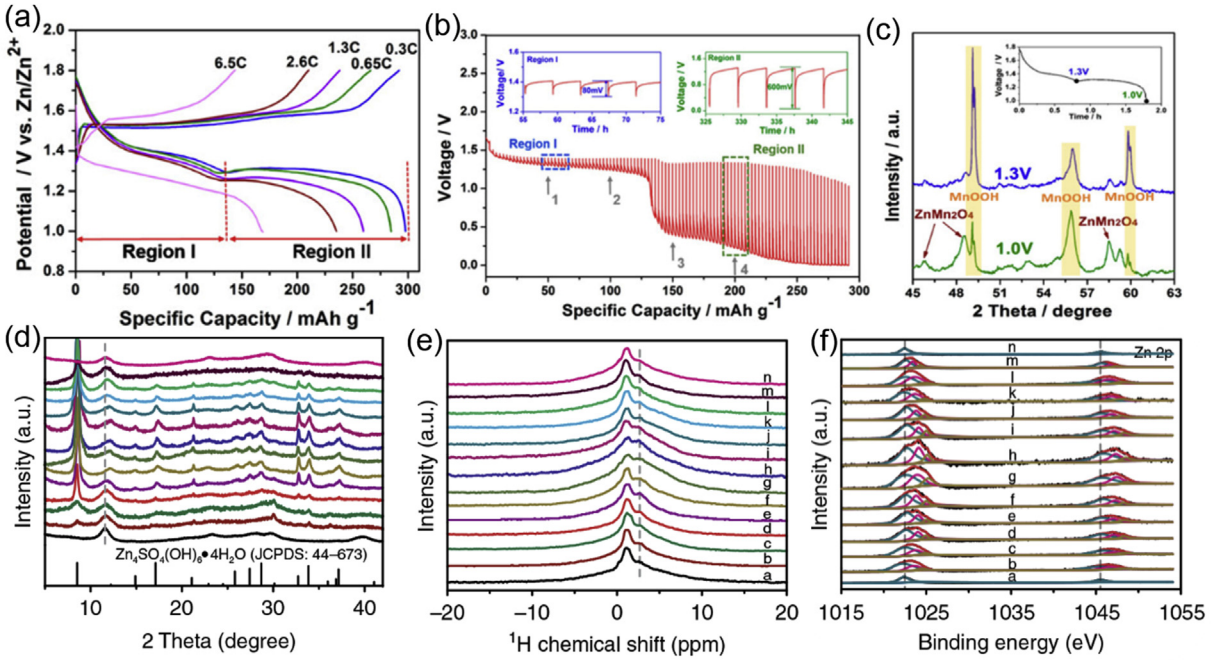

Fig. 3. (a) Charge and discharge curves of Zn/MnO_2@CFP cell at different rates in the first cycle. (b) Discharge galvanostatic intermittent titration technique (GITT) profiles of the Zn/MnO_2@CFP cell (50 mA/g for 120 s followed by a 4-h rest). (c) *Ex situ* XRD patterns of the MnO_2 @CFP cathode at the depth of discharge at 1.3 and 1.0 V, respectively [31]. (d) *Ex situ* XRD patterns, (e) solid-state ^{1}H nuclear magnetic resonance, and (f) XPS spectra of Zn 2p at selected states of $NaV_3O_8 \cdot 1.5H_2O$ electrodes [48].

both large voltage jump and slow ion diffusion in region II. Given strong electrostatic interactions with the host lattice and the large size of Zn^{2+}, H^+ insertion accounts for region I, and the Zn^{2+} insertion contributes to region II. The hypothesis is further proved by XRD measurements of MnO_2@CFP electrode after discharge to 1.3 and 1.0 V (Fig. 3c). Typical MnOOH peaks are observed after discharge to 1.3 V, whereas the $ZnMn_2O_4$ diffraction peaks can be observed only when discharged to 1.0 V, which also supports the consequent H^+ and Zn^{2+} co-insertion mechanism for akhtenskite MnO_2.

2.3.2. *Simultaneous Zn^{2+} and H^+ insertion/extraction mechanism*

Different from the step-wise H^+ and Zn^{2+} insertion/extraction into/from ϵ-MnO_2, Chen et al. [48] proposed simultaneous Zn^{2+} and H^+ insertion/extraction mechanism in Zn/sodium vanadate ($NaV_3O_8 \cdot 1.5H_2O$ [NVO]) system. *Ex situ* XRD analysis (Fig. 3d) depicts

the reversible and successive formation/decomposition of $Zn_4SO_4(OH)_6 \cdot 4H_2O$ on cathode during the charge/discharge process, which resulted from the continuous insertion/extraction of H^+ in/from the NVO. As displayed in Fig. 3e, an extra peak at 2.7 ppm ascribed to inserted H^+ increases gradually during discharge and recovers to the pristine state after charge, indicating the continuous and reversible insertion/extraction of H^+. In addition to the reversible insertion of H^+, Zn 2p peaks of NVO electrodes (1,023/1,046 eV) assigned to the inserted Zn^{2+} in NVO display a similar trend (Fig. 3f), suggesting consecutive and reversible insertion/extraction of Zn^{2+} in the NVO during discharge/charge. Thus, it is concluded that H^+ and Zn^{2+} can simultaneously insert/extract into/from NVO during discharge/charge based on the previous discussion.

2.4. Dissolution–deposition reaction mechanism

The aforementioned three mechanisms based on the reversible insertion/extraction of cations can only access one-electron redox reaction of Mn^{4+}/Mn^{3+}, rendering limited specific capacity of below 308 mAh/g and output voltages of below 1.8 V. Moreover, the specific capacity depends on the crystal structure of cathode materials and the type of insertion cations. Recently, the dissolution–deposition reaction mechanism was proposed in aqueous ZIBs [49–54]. In detail, the loaded MnO_2 cathode dissolves in the form of Mn^{2+} ions into the electrolyte during discharge, and the Zn anode is simultaneously oxidized into Zn^{2+} ions. The subsequent charge process follows the reverse evolution of discharge. The reaction mechanism can be described as follows:

$$\text{Cathode: } Mn^{2+} + 2H_2O - 2e^- \leftrightarrow MnO_2 + 4H^+ \quad E = 1.23\ \text{V vs. SHE} \quad (7)$$

$$\text{Anode: } Zn^{2+} + 2e^- \leftrightarrow Zn \quad E = -0.76\ \text{V vs. SHE} \quad (8)$$

The dissolution–deposition reaction mechanism involving two-electron reaction of MnO_2 endows the Zn–MnO_2 batteries with a high theoretical specific capacity of 616 mAh/g, a high working voltage of ~2 V, and higher energy density. In addition, a similar dissolution mechanism seems to apply to the Zn-vanadium oxide batteries, which needs further investigation.

3. Cathode materials

3.1. Manganese-based oxides

In the past decades, manganese oxides have been extensively used in many batteries because of their low cost, low toxicity, and multiple oxidation states of Mn. Open crystal structure with large crystal tunnels or layer spacings and a high operating voltage of ~1.3 V make manganese oxides as promising cathode materials of aqueous ZIBs.

3.1.1. MnO_2

Among them, MnO_2 composed of fundamental MnO_6 octahedra has the most crystallographic polymorphs, including α-, β-, γ-, λ-, and δ-MnO_2. The basic MnO_6 octahedra can be linked by sharing edges/corners, forming various MnO_2 polymorphs with tunnel/layered/spinel-type structures.

3.1.1.1. Tunneled structure. α-MnO_2 with large 2 × 2 tunnels (4.6 × 4.6 Å^2) can accommodate the reversible insertion/extraction of Zn^{2+} ions and thus become a research hotspot of cathode in ZIBs. Kang et al. [23,57] reported reversible intercalation of Zn^{2+} in the tunnels of α-MnO_2 (Fig. 4a). The Zn/α-MnO_2 battery delivers a specific capacity of 210 mAh/g with a discharge potential of 1.3 V and unsatisfactory lifespan of 100 cycles at 6C. Other studies show that α-MnO_2 exhibit similar operating voltage and discharge capacity.

Although Zn/α-MnO_2 batteries possess decent energy densities of 225 Wh/kg, they suffer from fast capacity fading during cycling and inferior performance at high rates. To address the issue, Lee

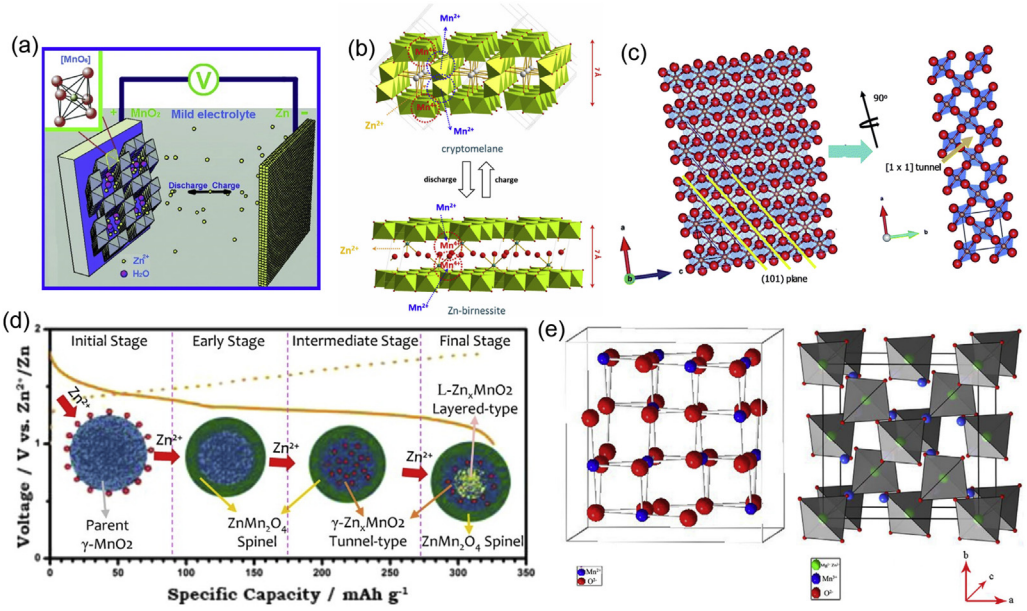

Fig. 4. (a) Schematic illustration of the chemistry of the zinc-ion battery. Zn^{2+} ions migrate between tunnels of an α-MnO_2 cathode and a Zn anode. The inset in the upper left corner shows the basic structural unit of the MnO_6 octahedron of MnO_2 [23]. (b) Schematic illustration of the mechanism of zinc intercalation into α-MnO_2. Green octahedra and white, red, and turquoise spheres represent MnO_6, K^+, H_2O, and Zn^{2+}, respectively [55]. (c) Illustration of the crystallographic structure of the β-MnO_2 nanorod sample. The [1 × 1] open tunnels in the β-MnO_2 nanorod are visible by rotating the nanorods approximately 90° along the a-axis [56]. (d) Schematic illustration of the reaction pathway of Zn insertion in the prepared γ-MnO_2 cathode [45]. (e) Crystal structure of λ-MnO_2 with void spaces after the removal of Li^+ and $ZnMn_2O_4$ after the intercalation of Zn^{2+} [46].

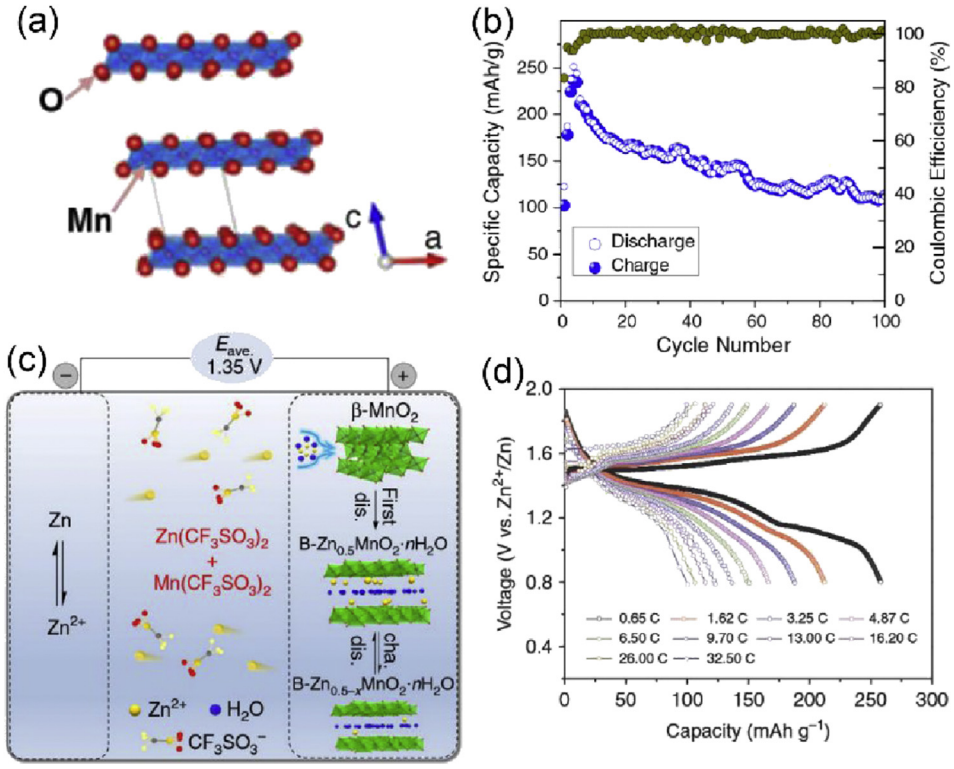

Fig. 5. (a) Crystallographic structure of δ-MnO_2. (b) Cyclability and Coulombic efficiency of Zn/δ-MnO_2 battery at 83 mA/g [47]. (c) Schematic illustration of Zn^{2+} insertion/extraction in layered Zn-buserite. (d) Discharge/charge profiles of Zn/Zn-buserite cells at varying C rates [44].

et al. [55] elucidated the reaction mechanism between α-MnO_2 and zinc ions during discharge/charge. With the electrochemical intercalation of Zn^{2+}, the highly unstable Mn^{3+} formed by the reduction of Mn^{4+} disproportionates into Mn^{4+} and Mn^{2+}, leading to the dissolution of manganese into the electrolyte and phase transition from tunneled structure to layered Zn-birnessite (Fig. 4b). Upon charging, Mn^{2+} ions incorporate with layers of Zn-birnessite to recover the original tunneled structure. In 2016, the cycling performance of α-MnO_2 nanowires based on conversion reaction mechanism were significantly improved (92% capacity retention after 5,000 cycles) by adding 0.1M $MnSO_4$ into $ZnSO_4$ electrolyte to inhibit dissolution of α-MnO_2 [26].

β-MnO_2 has the narrowest (1 × 1) tunnel (2.3 × 2.3 $Å^2$) compared with other tunnel-type MnO_2 polymorphs, which is not conducive to the intercalation/deintercalation of Zn^{2+} [23]. Kim et al. [56] claimed that β-MnO_2 nanorods with exposed (101) planes (Fig. 4c) possess good Zn^{2+} storage capability (270 mAh/g at 100 mA g^{-1}, 75% capacity retention over 200 cycles at 200 mA/g) in 1M $ZnSO_4$ aqueous electrolyte in contrast to its inactive bulk counterpart. However, β-MnO_2 undergoes phase transition to form a layered Zn-buserite in 3M $Zn(CF_3SO_3)_2$ + 0.1M $Mn(CF_3SO_3)_2$ aqueous electrolyte during the initial discharge, which greatly improves the reversible capacity and cycling stability of cathode [44].

γ-MnO_2 with irregular (1 × 1, 2.3 × 2.3 $Å^2$) and (1 × 2, 2.3 × 4.6 $Å^2$) tunnels has been demonstrated to be a suitable cathode for the aqueous ZIBs [45,58]. Kim et al. [45] reported that mesoporous γ-MnO_2 cathode exhibits a discharge capacity of 285 mAh/g at 0.05 mA/cm^2 with a defined plateau at ~1.25 V vs. Zn/Zn^{2+}. *In situ* synchrotron X-ray absorption near edge structure (XANES) and XRD studies revealed the complex phase transition of γ-MnO_2 with the insertion of Zn^{2+}. After full discharge, the γ-MnO_2 undergoes a structural transformation to spinel-type $ZnMn_2O_4$, tunnel-type γ-Zn_xMnO_2, and layered-type L-Zn_yMnO_2 phases, accompanied by the reduction of manganese from Mn(IV) to the Mn(III) and Mn(II) states, respectively (Fig. 4d). On subsequent charging, a majority of structural variations revert back to the parent γ-MnO_2 with the extraction of Zn^{2+}.

3.1.1.2. Spinel structure. λ-MnO_2 with the limited 3D tunnels seems to be unfit for the diffusion of Zn^{2+} ions [23]. Later, Cao et al. [46] investigated the electrochemical performance of λ-MnO_2 synthesized via leaching $LiMn_2O_4$ in H_2SO_4 (Fig. 4e). The λ-MnO_2 delivered a specific capacity of 442.6 mAh/g at 13.8 mA/g and 33.8 mAh/g at 408 mA/g in aqueous $ZnSO_4$ electrolyte.

3.1.1.3. Layered structure. The birnessite δ-MnO_2 consists of loosely bound layers of edge-shared [MnO_6] octahedra situated on the (001) plane of the structure (Fig. 5a). The (001) plane has a large interlayer distance of ~0.7 nm, which is theoretically feasible for Zn ion insertion and extraction. Kim et al. [47] reported the δ-MnO_2 nanoflakes synthesized by the facile thermal decomposition of $KMnO_4$ as positive electrode for aqueous ZIBs. At a current density of 83 mA/g, the δ-MnO_2 cathode delivered first discharge capacity of 122 mAh/g and increased to 252 mAh/g in the fourth cycle, and decreased to 112 mAh/g after 100 cycles with Coulombic efficiencies approaching 100% (Fig. 5b). The layer-type δ-MnO_2 transforms to spinel-type $ZnMn_2O_4$ and layered-type δ-Zn_xMnO_2 with the insertion of Zn^{2+} during discharge. The presence of $ZnMn_2O_4$ with the Jahn–Teller Mn^{3+} ion may lead to structural degradation, thus resulting in fast capacity fade on repeated cycling.

Buserite possesses a two-dimensional layered structure, which forms MnO_2 sheets of edge-sharing MnO_6 octahedra assembled in layers and two sheets of water molecules and metal ions in the interlayer region. The large basal spacing of ~ 10 Å and two sheets of interlayer water molecules can accommodate a large amount of electrolyte cations and provide more favorable pathways for

electrolyte cations intercalation and deintercalation [59,60]. Chen et al. [44] reported layered Zn-buserite prepared by electrochemical phase transition from tunneled α, β, and γ MnO_2 in 3M $Zn(CF_3SO_3)_2$ + 0.1M $Mn(CF_3SO_3)_2$ aqueous electrolyte as cathode for ZIBs. In the case of β-MnO_2, the initial cyclic voltammetry (CV) profile differs from subsequent cycles, suggesting β-MnO_2 undergoes phase transition. On first discharging, the XRD peaks of β-MnO_2 gradually diminish and new peaks emerging at 6.47, 13.00, 19.58, 26.28, and 32.93° correspond to reflections from the (001)–(005) crystallographic planes of layered Zn-buserite phase. After 10 cycles, XRD signal of β-MnO_2 is not discernible. In the following cycles, Zn^{2+} reversibly insert/extract in/from the layered structure (Fig. 5c). The Zn-buserite cathode delivers a high discharge capacity of 225 mAh/g, good rate capability (Fig. 5d), and long-term cycling stability with 94% capacity retention after 2,000 cycles.

3.1.2. Other manganese-based oxides

Other viable manganese oxides such as MnO, Mn_2O_3, and Mn_3O_4 were also investigated as cathode materials of ZIBs. In general, manganese oxide containing manganese ion at the lower valence state (MnO [61], Mn_2O_3 [62], and Mn_3O_4 [63,64]) would undergo irreversible phase transition to stable MnO_2 during initial electrochemical cycles, followed by reversible Zn^{2+}/H^+ insertion and extraction in/from transformed MnO_2.

3.2. Vanadium-based cathodes

Open framework, multivalence of vanadium, and easy availability make V-based compounds as promising candidates for cathode materials of aqueous ZIBs. The last three years have witnessed significant progresses in the development of V-based cathode materials, which involves vanadium oxides, vanadates, vanadium sulfides, and vanadyl phosphates. Among them, vanadium oxides (V_2O_5, VO_2, V_3O_7 H_2O, V_6O_{13}, and $V_{10}O_{24}{\cdot}12H_2O$), vanadates ($M_xV_nO_m$), and vanadium sulfides (VS_2, V_3S_4) exhibit similar operating voltage of ~0.7 V, while vanadyl phosphates ($Na_3V_2(PO_4)_3$, $VOPO_4$) possess high discharge potential of 1.2–1.4 V.

3.2.1. Vanadium oxide

3.2.1.1. V_2O_5. Orthorhombic V_2O_5 comprises square pyramid layers built by edge- and corner-sharing VO_5 pyramids. The large interlayer space of (200) plane is 0.58 nm, which is beneficial for Zn^{2+} insertion/extraction.

In 3M $ZnSO_4$ aqueous electrolyte, the interlayer space of (200) plane enlarges to 0.63 nm due to the insertion of Zn^{2+}. The Zn/V_2O_5 battery delivers low reversible capacity (224 mAh/g at 0.1 A/g) and unsatisfactory cycle life (400 cycles at 1 A/g and at 2 A/g) [67]. However, in 3M $Zn(CF_3SO_3)_2$ aqueous electrolyte, orthorhombic V_2O_5 gradually transforms to bilayered V_2O_5 with the co-insertion/extraction of Zn^{2+} and water (Fig. 6a), accounting for the initial increasing in discharge capacity [34]. Benefiting from the phase transition and morphological evolution, the electrochemical performance of the Zn/V_2O_5 battery was significantly improved. A high capacity of 470 mAh/g was delivered at 0.2 A/g (Fig. 1b), and a high energy density (274 Wh/kg at 7,100 W/kg) with satisfactory long-term cyclability (91.1% capacity retention over 4,000 cycles at 5 A/g) were simultaneously achieved. Bilayer V_2O_5 with crystal water in the interlayers has a large interlayer spacing (>10 Å), is a promising candidate for Zn^{2+} intercalation. The co-inserted water can

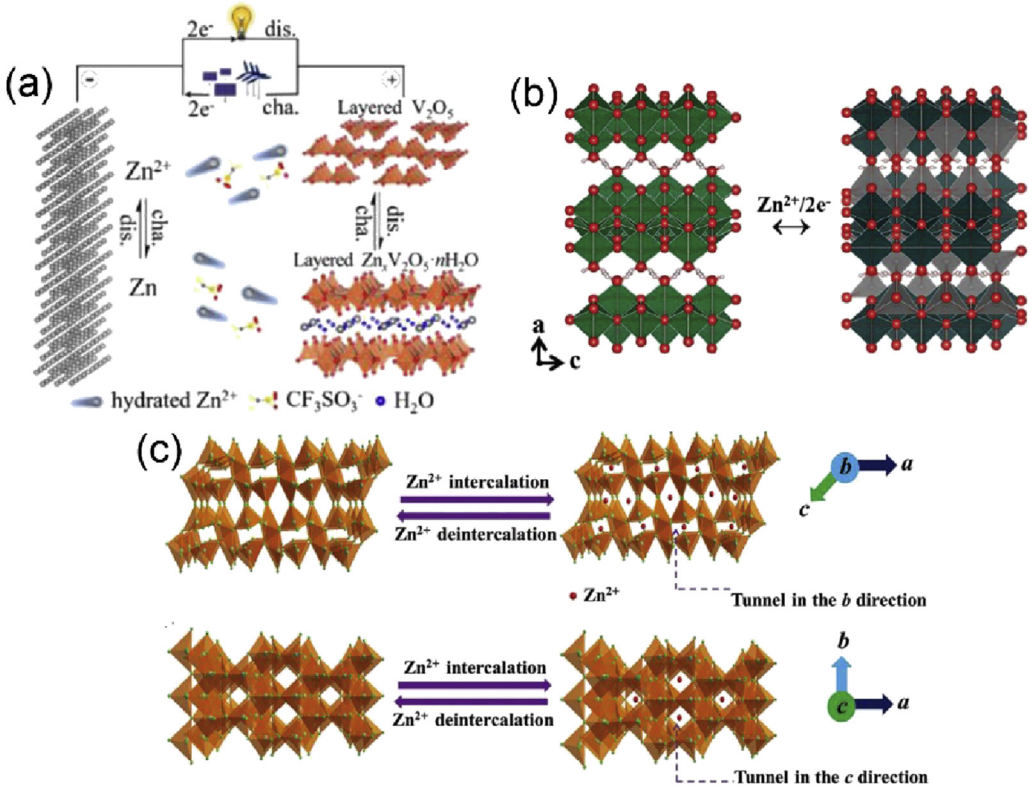

Fig. 6. (a) Schematic illustration of the rechargeable aqueous Zn/V_2O_5 battery chemistry [34]. (b) Crystal structure viewed along the [010] direction showing the large interlayer gallery between V_3O_7 sheets perpendicular to the [100] direction for Zn^{2+} intercalation. VO_x polyhedra are depicted in green and blue for the pristine and the Zn^{2+} intercalated materials, respectively. ZnO_x polyhedra, gray; O, red spheres [65]. (c) Schematic view of Zn^{2+} intercalation/de-intercalation VO_2 (B) nanofibers projected along the direction of the b- and c-axes, respectively [66].

lubricate the transportation of Zn^{2+} and the structural water effectively screens electrostatic interactions with the V_2O_5 framework, leading to fast kinetics and good cycling stability [38]. The Zn/$V_2O_5 \cdot nH_2O$/graphene battery shows superior rate performance (248 mAh/g at 30 A/g) and long-term cycling stability (71% capacity retention after 900 cycles at 6 A/g).

3.2.1.2. $V_3O_7{\cdot}H_2O$ ($H_2V_3O_8$). $V_3O_7 \cdot H_2O$ ($H_2V_3O_8$) consists of 2D V_3O_8 layers stacked along the a-axis by hydrogen bonding between H_2O molecule and VO_6 octahedra, yielding a 3D structure (Fig. 6b). The high electrical conductivity stemming from mixed valence of vanadium ($V^{4+}/V^{5+} = 1/2$) and weak hydrogen bonds between V_3O_8 layers endow $V_3O_7 \cdot H_2O$ ($H_2V_3O_8$) with the capability to store Zn^{2+} [65,68,69].

He et al. [68] constructed Zn/$H_2V_3O_8$ nanowires battery with $Zn(CF_3SO_3)_2$ aqueous electrolyte, which delivers a high discharge capacity of 423.8 mAh/g at 0.1 A/g and good cycling stability with 94.3% capacity retention after 1,000 cycles at 5.0 A/g. The decent electrochemical performance can be attributed to a slight change of the structure during the intercalation/de-intercalation of Zn^{2+} due to the large interlayer spacing of $H_2V_3O_8$. Thus, exploring materials with large interlayer spacing may be an effective strategy to enhance the cyclic stability of cathodes for ZIBs. Nazar et al. [65] reported that layered $V_3O_7 \cdot H_2O$ delivers high specific capacity of 275–375 mAh/g at 1C–8C in aqueous electrolytes, while it exhibits low capacity and rate capabilities in non-aqueous medium. Operando XRD studies, combined with impedance analysis, reveal that high desolvation penalty and strong Coulomb repulsion at the interface are the origin of poor electrochemical performance in the non-aqueous electrolyte.

3.2.1.3. VO_2. Vanadium dioxide (VO_2 (B)) constructed by distorted VO_6 octahedra sharing both corners and edges has big tunnels (0.82, 0.34, and 0.5 nm^2 along the b-, a-, and c-axes), which favors fast insertion/extraction of ions. Yang et al. [66] demonstrate a novel intercalation pseudocapacitance behavior and ultrafast kinetics of Zn^{2+} in VO_2 (B) nanofibers in aqueous $Zn(CF_3SO_3)_2$ electrolyte via various electrochemical analyses and *in situ* XRD. Unique tunnel transport pathways and little structural change of VO_2 with Zn^{2+} intercalation/deintercalation avoid the limitation from solid-state diffusion in the VO_2 electrode (Fig. 6c). As a consequence, VO_2 (B) nanofibers exhibit a high discharge capacity of 357 mAh/g and the highest rate capability (171 mAh/g at 300C) for aqueous ZIBs. The monoclinic VO_2 with layered structure formed by edge-sharing VO_6 octahedra is also potential intercalation host for Zn^{2+}. Recently, Wang et al. [70] revealed an electrochemical phase transition from the metastable VO_2 to bilayered $V_2O_5 \cdot nH_2O$, which is induced by the initial insertion/extraction of Zn^{2+} in VO_2. Thanks to the enlarged interlayer spacing and enhanced structural stability, the battery exhibits decent cycling stability (capacity retention of 79% after 10,000 cycles) and high energy density of 271.8 W h/kg.

3.2.2. Vanadates

Various metal ions and low molecular weight compounds can be preintercalated into the interlayer of vanadium oxides, forming vanadates. In this regard, vanadates can be seen as derivatives of vanadium oxides and classified into $M_xV_2O_5$, $M_xV_3O_8$, $M_xV_2O_7$, and so on, according to different frameworks of vanadium oxides. Herein, several representative vanadates as cathode materials of aqueous ZIBs are discussed.

3.2.2.1. $M_xV_2O_5$. $M_xV_2O_5$ (M = metal ion) with preintercalated ions such as alkali metal ions (Li^+, Na^+, and K^+) [74,75], alkali earth

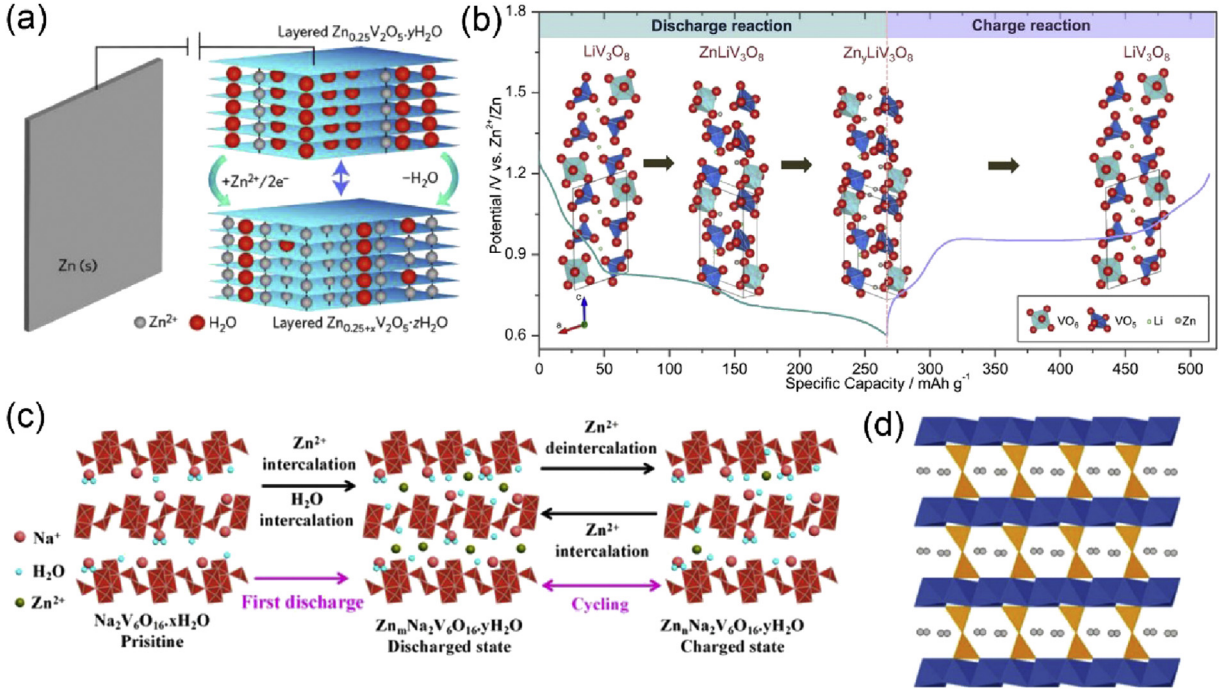

Fig. 7. (a) Schematic illustration of the Zn/$Zn_{0.25}V_2O_5$ cell on discharge in 1M $ZnSO_4$ aqueous electrolyte, showing the expanded interlayer arrangement owing to incorporation of additional water molecules between the V_2O_5 layers (represented by the blue sheets) [8]. (b) Schematic illustration of the Zn-intercalation mechanism in the present LiV_3O_8 cathode [71]. (c) Schematic illustrations of water intercalation accompanying Zn^{2+} intercalation into $Na_2V_6O_{16} \cdot xH_2O$ at the first discharge process and Zn^{2+} deintercalation and intercalation upon electrochemical charge and discharge processes (here, x < y and m > n) [72]. (d) Crystal structure viewed along the b-axis of $Zn_3V_2O_7(OH)_2 \cdot 2H_2O$, which shows a layered structure with porous framework. The Zn atoms in ZnO_6 and V atoms in V_2O_7 polyhedra are depicted in blue and yellow, respectively. The gray atoms in the crystal cavities represent the lattice water [73].

metal ions (Mg^{2+} and Ca^{2+}) [36,76], and transition metal ions (Zn^{2+}, Mn^{2+}, etc.) [8,77,78], as well as crystal water in V_2O_5 bilayers have robust architectures with facile zinc-ion pathways.

In 2016, $Zn_{0.25}V_2O_5 \cdot nH_2O$ nanobelts synthesized by scalable microwave approach was first investigated as cathode materials of ZIBs [8]. As illustrated in Fig. 7a, the indigenous Zn ions and structural water act as pillars to stabilize the layered structure, ensuring structural stability during cycling. According to the XRD analysis, the co-intercalated water plays a vital role in reversibly expanding and contracting the interlayer space of $Zn_{0.25}V_2O_5 \cdot nH_2O$ during Zn^{2+} ingress/egress, accounting for good kinetics. Robust structural features with large interlayer space and stable layered host pillared by indigenous Zn ions and structural water act in concert to render high rate capability (183 mAh/g at 20C) (Fig. 4b) and long-term cyclability (>1,000 cycles). Compared to $Zn_{0.25}V_2O_5 \cdot nH_2O$, $Ca_{0.24}V_2O_5 \cdot nH_2O$ (CVO) is a more suitable aqueous ZIB intercalation cathode owing to the lager interlayer space (14.1 Å) caused by longer Ca—O bonds in CaO_7 pillars, fourfold higher electrical conductivity and lower molecular weight and density [36]. The CVO cathode delivers a high capacity of 340 mAh/g at 0.2C, excellent rate capability, and long cycling life (96% retention after 3,000 cycles at 80C). The Zn/CVO cells display an impressive energy density of 267 Wh/kg at a power density of 53.4 W/kg, superior to most of the previously reported cathodes. Moreover, *ex situ* XRD, XPS, and TEM analysis elucidate the reversible Zn^{2+} intercalation mechanism during charge/discharge.

Recently, Zheng et al. [78] made a breakthrough in the cycle life of $M_xV_2O_5$ cathodes. They design a 3D porous $Zn_{0.3}V_2O_5 \cdot 1.5H_2O$ (ZVO) nanoflowers by electrochemical phase transition from VOOH hollow nanospheres during cycling in $Zn(CF_3SO_3)_2$ aqueous electrolyte. The 3D hierarchical porous structure renders abundant contact with electrolyte, shortens the ion diffusion path, and provides cushion for relieving strain generated during electrochemical processes. The synchronous Zn^{2+}/H^+ ion insertion preserves the V_2O_5 interlayer spacing, and preintercalated zinc ions and crystal water residing in interlayers stabilize the host structure, ensuring long-term cycling stability. As a consequence, the Zn/ZVO battery displays a high specific capacity of 426 mAh/g at 0.2 A/g and a long-term cycling stability with 96% capacity retention after 20,000 cycles at 10 A/g, which is the longest cycle life of reported aqueous ZIBs.

3.2.2.2. $M_xV_3O_8$. Layered $M_xV_3O_8$ have also been extensively studied as cathode materials of ZIBs in the past 3 years. In $M_xV_3O_8$, V_3O_8 layers constructed by corner-shared VO_6 octahedra and VO_5 square pyramids stack along the z-axis and metal ions between the layers serve as links and pillars to stabilize the structures.

Kim et al. [71] unraveled the phase evolution of LiV_3O_8 during Zn (de)intercalation by *in situ* XRD, electrochemistry, and simulation techniques. During discharge, LiV_3O_8 exhibited a solid-solution behavior at the initial stage, followed by the two-phase reaction involving the stoichiometric $ZnLiV_3O_8$ phase in the intermediate stage and the subsequent solid-solution behavior of the $Zn_yLiV_3O_8$ ($y \geq 1$) at the final stage (Fig. 7b). In the consecutive charge process, the $Zn_yLiV_3O_8$ transforms directly to LiV_3O_8 via a single-phase behavior. As to $Na_2V_6O_{16} \cdot xH_2O$ ($2(NaV_3O_8 \cdot x/2H_2O)$) with large interplanar spacing of 0.79 nm, structured water plays a significant role in improving electrochemical performances (Fig. 7c), especially the cycling stability based on electrochemical characterizations, XRD and XPS analysis [72]. The $Na_2V_6O_{16} \cdot xH_2O$ cathode displays a high specific capacity of 352 mAh/g at 50 mA/g, decent rate performance and long-term cyclic stability with a capacity retention of 90% after 6,000 cycles.

3.2.2.3. $M_xV_2O_7$. Zinc pyrovanadate ($Zn_2V_2O_7$ or $Zn_3V_2O_7(OH)_2 \cdot 2H_2O$) is built up of zinc oxide layers pillared by (V_2O_7) groups and water molecules along the z-axis (Fig. 7d). Such an open-framework with large interlayer spacing of 0.719 nm is favorable for electrochemical insertion/extraction of Zn^{2+} ions. The $Zn_3V_2O_7(OH)_2 \cdot 2H_2O$ nanowires cathode delivers high capacities of 213 and 76 mAh/g at 50 and 3,000 mA/g, and good cycling stability up to 300 cycles with 68% capacity retention [73]. Kim et al. [79] revealed multistep Zn^{2+} insertion/extraction into/from layered α-$Zn_2V_2O_7$ nanowires by the post-mortem analysis. The α-$Zn_2V_2O_7$

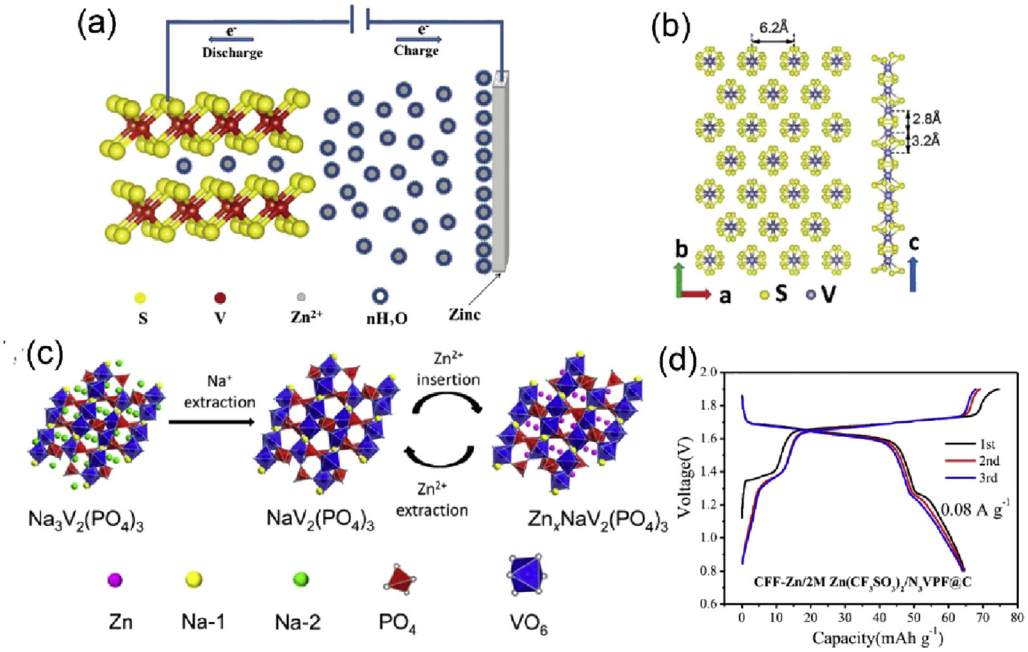

Fig. 8. (a) Schematic illustration of the operation mechanism of Zn/VS_2 batteries [33]. (b) Crystal structure of VS_4 [80]. (c) Schematic representation for phase transition of $Na_3V_2(PO_4)_3$ cathode during cycling [32]. (d) Initial three charge/discharge profiles of CFF-Zn/$Na_3V_2(PO_4)_3$F@C battery at 0.08A/g^{-1} [81].

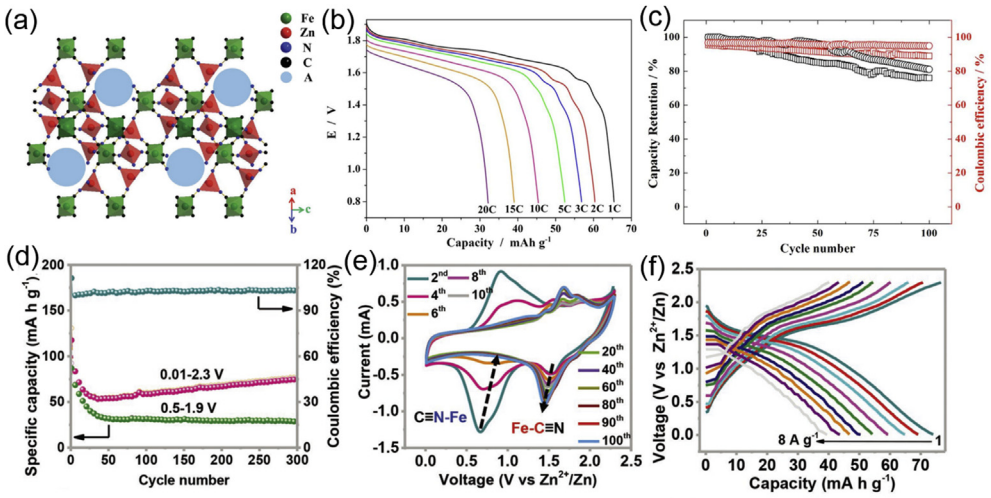

Fig. 9. (a) Crystal structure of rhombohedral zinc hexacyanoferrate. (b) Rate capability of the Zn/ZnHCF battery. (c) Cycle life tests of the Zn/ZnHCF battery at a rate of 1C (square) and 5C (circle) (1C = 60 mA/g, 5C = 300 mA/g) [29]. (d) Cycling performance operated at two different voltage windows. (e) *In situ* CV curves recorded at 2 mV/s. (f) Rate capability of Zn/FeHCF batteries [84].

nanowires exhibit excellent rate capability due to high capacitive contribution in the total current response and good cyclic stability with 85% capacity retention after 1,000 cycles at 4,000 mA/g.

3.2.3. Vanadium sulfides

Vanadium sulfides such as VS_2 and VS_4 have large interlayer spacing, enabling the facile insertion/extraction of Zn^{2+} ions (0.74 Å) [33,80,82]. VS_2 has a kind of sandwich structure with an interlayer spacing of 5.76 Å, which comprises a vanadium layer between two sulfur layers (Fig. 8a). During discharge, 0.09 Zn^{2+} ions insert into layers of VS_2 to form conductive $Zn_{0.09}VS_2$, followed by the phase change from $Zn_{0.09}VS_2$ to $Zn_{0.23}VS_2$ with the insertion of Zn^{2+} ions [33]. Combined with the superior conductivity of rGO, VS_4 with a large interlayer spacing of 5.6 Å (Fig. 8b) exhibits a high capacity of 180 mAh/g at 1 A/g and excellent rate performance (83.7% capacity retention from 0.2 A/g to 2 A/g) [80].

3.2.4. Vanadyl phosphates

Vanadium phosphates with NASICON structure have large channels and fast ion diffusion coefficients and have been studied as storage guests for Zn^{2+} ions [32,81,83]. Huang et al. [32] reported that graphene-like carbon-wrapped $Na_3V_2(PO_4)_3$ (NVP/C) nanoparticles deliver a specific capacity of 97 mAh/g at 0.5C with a discharge plateau of 1.1 V and retains 74% capacity after 100 cycles. The original NVP transforms to $NaV_2(PO_4)_3$ after two Na^+ ions are extracted from NVP during the first charge process (Fig. 8c). In subsequent cycles, Zn^{2+} ions reversibly intercalate/deintercalate into/from $NaV_2(PO_4)_3$ accompanied by the reduction/oxidation of V. Later, Jiang et al. [81] investigated another prototype of NASICON-typed $Na_3V_2(PO_4)_2F_3$, which has more stable structure because of the strong affinity of F atoms toward the surroundings. When evaluated as cathode materials of ZIBs, $Na_3V_2(PO_4)_2F_3$ exhibits a high voltage output of 1.62 V (Fig. 8d) and remarkable cycling stability with 95% capacity retention over 4,000 cycles at 1 A/g.

3.3. PBA

PBAs have a typical face-centered cubic structure, in which the Fe(III)C_6 octahedra are linked to M(II)N_4 tetrahedra (M = Ni^{2+}, Cu^{2+}, Zn^{2+}, etc.) via CN ligands to form a porous 3D framework with large open A sites containing alkaline cations (Na^+, K^+, and Cs^+) and zeolitic water (Fig. 9a). Such an open framework with large interstitial sites allows facile and reversible insertion/extraction of ions, endowing PBAs with the potential to serve as intercalation hosts for various cations, including Zn ions [27–30,84].

In 2015, Trocoli and La Mantia [30] first reported CuHCF ($CuFe(CN)_6$) as cathode materials of ZIBs in aqueous 20mM $ZnSO_4$ electrolyte. The battery exhibits 90% of the theoretical capacity with an average discharge potential of 1.73 V and a capacity retention of 96.3% after 100 cycles at 1C. In addition, the specific power at 10C of the Zn/CuHCF battery is comparable to those of organic batteries with $Li_4Ti_5O_{12}$ and $LiFePO_4$ cathodes. Liu et al. [29] also reported another PBA ZnHCF ($Zn_3[Fe(CN)_6]_2$) as intercalation hosts for Zn^{2+}. The electrochemical behaviors of ZnHCF are subject to the cations (Na^+, K^+, and Zn^{2+}) in Na_2SO_4, K_2SO_4, and $ZnSO_4$ aqueous electrolytes. ZnHCF exhibits higher discharge potential in aqueous Na_2SO_4/K_2SO_4 electrolytes because of the larger ionic radii of Na^+/K^+, whereas ZnHCF keeps more stable in aqueous $ZnSO_4$ electrolyte. In aqueous $ZnSO_4$ electrolyte, it delivers a discharge capacity of 65.4 mAh/g at 1C with an average discharge voltage of ~1.7 V (Fig. 9b) and good cycling stability with capacity retention over 81% after 100 cycles at 5C (Fig. 9c). The Zn/$ZnSO_4$/ZnHCF battery exhibits the second highest recorded average operational voltage (ca. 1.7 V) among aqueous metal-ion batteries and achieves a specific energy density of 100 Wh/kg based on the total mass of active electrode materials. As for FeHCF, the specific capacity involves the redox reaction of high-spin Fe (III) coordinated with N atoms at a low voltage of ≈0.1 V vs. Ag/AgCl and the low-spin Fe(III) coordinated with C atoms at a high voltage of ≈0.8 V [11]. Zhi et al. [84] demonstrated that high-voltage scanning can effectively activate the low-spin Fe of FeHCF. Benefiting from the high-voltage activation (Fig. 9d&e), the Zn/FeHCF hybrid-ion achieved an excellent rate capability of maintaining 53.2% capacity at an ultra-high current density of 8 A/g (≈97C) (Fig. 9f). Furthermore, a record-breaking cycling performance of 73% capacity retention after 10,000 cycles with coulombic efficiency approaching 100% was realized.

In short, despite operating at relatively high average operating voltage (about 1.7 V vs. Zn), PBAs deliver limited specific capacity of less than 80 mAh/g because of the occupation of large amount of hexacyanoferrate vacancies and the interstitial water in their structures, resulting in low energy density. Furthermore, they

suffer from O_2 evolution because of the high operating voltage (about 1.7 V vs. Zn).

3.4. Organic compounds and other cathodes

In addition to inorganic materials, organic compounds including polyaniline (PANI) [85,86], 9,10-di (1,3 dithiol-2-ylidene)-9,10-dihydroanthracene (exTTF) [40], poly (benzoquinonyl sulfide) (PBQS) [87], tetrachloro-1,4-benzoquinone (*p*-chloranil) [88], and calix [4]quinone (C4Q) [39] have also been applied as cathode materials of ZIBs because of their light weight, sustainability, and environmental benignity.

In 2016, Schubert et al. [40] reported 9,10-di (1,3-dithiol-2-ylidene)-9,10-dihydroanthracene (exTTF) as active cathode materials for ZIBs. The cathode exhibited chemically reversible two-electron redox reaction in 1M aqueous $Zn(CF_3SO_3)_2$ electrolyte, leading to a theoretical capacity of 133 mAh/g with average discharge potential of 1.1 V (Fig. 10a). The battery featured high rate performance (up to 120C) and an ultra-long lifetime (over 10,000 cycles with 86% capacity retention) (Fig. 10b). Ubiquitous quinones have been found to serve as sustainable and green electrode materials for aqueous batteries [39,89]. Energy storage of quinones is generally based on an 'ion-coordination' mechanism that positively charged cations coordinate with negatively charged oxygen atoms of carbonyl groups accompanied by the reduction of carbonyl groups. With open bowl structures and eight carbonyls as active sites, calix[4]quinone (C4Q) exhibits a high capacity of 335 mAh/g (corresponding to uptake of three Zn ions [Zn_3C4Q] and utilization of six carbonyls [Fig. 10c]) with a flat operating voltage of 1.0 V and a low polarization of 70 mV at 20 mA/g (Fig. 10d), and achieves a long life of 1,000 cycles with 87% capacity retention at 500 mA/g in 3M aqueous $Zn(CF_3SO_3)_2$ electrolyte [39]. However, an expensive Nafion film must be introduced in the Zn/C4Q system to prohibit the dissolution of discharge products and protect zinc anodes from poisoning by quinones.

The organic cathode materials with good mechanical stability and flexibility hold great promise in application of flexible ZIBs. Nevertheless, they are still in their infancy and research efforts on achieving higher capacity and energy density are desirable.

4. Challenges and strategies for better performance

The comprehensive electrochemical performances of the aforementioned cathode materials are unsatisfactory and need to be improved. They encounter some common issues of structural transformation and collapse, sluggish diffusion kinetics, low energy density, and serious degradation of ion storage capability at high mass loading, which greatly hamper the practical applications of aqueous ZIBs.

4.1. Nanostructure regulating

Bulk cathode materials suffer from sluggish Zn^{2+} diffusion kinetics and limited interfacial charge transfer because of the strong electrostatic interaction and inadequate contact between electrolyte and electrodes, resulting in inferior electrochemical properties in terms of specific capacity, rate capability, and cycle stability. The Zn^{2+} storage capability of electrode materials can be improved by tailoring their size and shape. Nanostructure engineering is an effective approach to boost the electrochemical performances of cathode materials. The nanostructured cathode materials feature small building blocks, large specific surface, and robust secondary configuration [90]. Specifically, nano-sized electrode materials with large surface area offer more active sites and interpenetrating electron/ion transport paths, which is beneficial to accelerate the reaction kinetics and decrease interfacial polarization, thus enabling high rate capability. Furthermore, the robust structure is favorable for the integrity of the electrode during cycle, achieving good cycling stability. The cathode materials with low-dimensional nanostructures (0D nanoparticles [14,30], 1D nanowires/nanobelts/nanofibers [8,26,36,72], and 2D nanoplates/nanosheets/nanoflakes [31,34,91]) exhibit decent Zn^{2+} storage properties. 3D hierarchical nanostructures with large interior voids integrate the merits of micrometer-scale materials and low-dimensional nanostructures, favoring the inhibition of agglomeration and fast diffusion of Zn^{2+}/H^+ ions. Moreover, 3D hierarchical architectures can alleviate the strains arising from Zn^{2+}/H^+ (de)intercalation, rendering good cycling stability of electrodes [78].

4.2. Structural stability improvement

4.2.1. Preintercalation of guest species

The cycling stability of the cathode is plagued by structural degradation and irreversible phase changes during the discharge/charge processes. Preintercalation of guest species (e.g. metal ions, water molecules, organic molecules, and organometallic molecules) into the cathode materials as pillars has proved to be effective to stabilize the host structure and facilitate ion diffusion [8,36,74,91,92].

δ-MnO_2 cathode failed to exhibit its potentially superior performance because of the frustrating structural degradation during charge/discharge cycles. To address the bottlenecks of Zn/δ-MnO_2 batteries, Zhi et al. [91] synthesized $Na_{0.44}Mn_2O_4 \cdot 1.5H_2O$ with an interlayer distance of 0.72 nm. Benefiting from Na ions and water molecule pillaring the host structure, Zn ion can diffuse smoothly and rapidly in the preintercalated layer (Fig. 11a). As a result, the Zn/δ-MnO_2 battery delivered extraordinary electrochemical performance. The battery achieves an energy density of 374 Wh/kg at 1C and endures 10,000 charging cycles with a capacity retention of 98% at 20C, superior to all previously reported α-, β-, γ-, and δ-MnO_2 cathodes. $Li_XV_2O_5 \cdot nH_2O$ (LVO-250) with the chemical intercalation of Li^+ in the interlayer of $V_2O_5 \cdot nH_2O$ (VO-250) has a larger spacing of 13.77 Å and higher diffusion coefficient of Zn^{2+} (D) (0.33×10^{-8} to 3.4×10^{-8} cm^2/s) than VO-250 [74]. The enlarged layer spacing and fast Zn^{2+} diffusion endow the Zn/LVO-250 battery high rate capacity and excellent cycling performance (192 mAh/g after 1,000 cycles at 10 A/g). In contrast with the superior electrochemical performance of LVO-250, VO-250 without the pillaring of Li^+ in the interlayer shows poor performance.

4.2.2. Introduction of electrolyte additives

In addition, structural transformation and collapse of cathode materials during cycling would lead to cathode dissolution, thus giving rise to rapid capacity decay. Recent studies demonstrate that pre-addition of relevant salts in electrolyte is an effective strategy to inhibit cathode dissolution and improve the electrochemical performance of aqueous ZIBs.

The pre-addition of Mn salt in the electrolyte is a common strategy to inhibit dissolution of MnO_2 polymorphs. For example, rapid capacity deterioration was observed in the Zn/α-MnO_2 battery with 2M $ZnSO_4$ electrolyte because of the dissolution of Mn^{2+} from Mn^{3+} disproportionation into the electrolyte during cycling. Liu et al. [26] pre-added an optimum concentration of 0.1M $MnSO_4$ into the $ZnSO_4$ electrolyte to reach an appropriate equilibrium between Mn^{2+} dissolution from α-MnO_2 electrode and the re-oxidation of Mn^{2+} in the electrolyte, leading to the high stability of α-MnO_2 electrode without affecting the redox reactions in the electrodes (Fig. 11b&c). A high capacity retention of 92% was achieved after 5,000 cycles, indicating $MnSO_4$ additive effectively improves the cycling stability of Zn/MnO_2 battery. The approach of

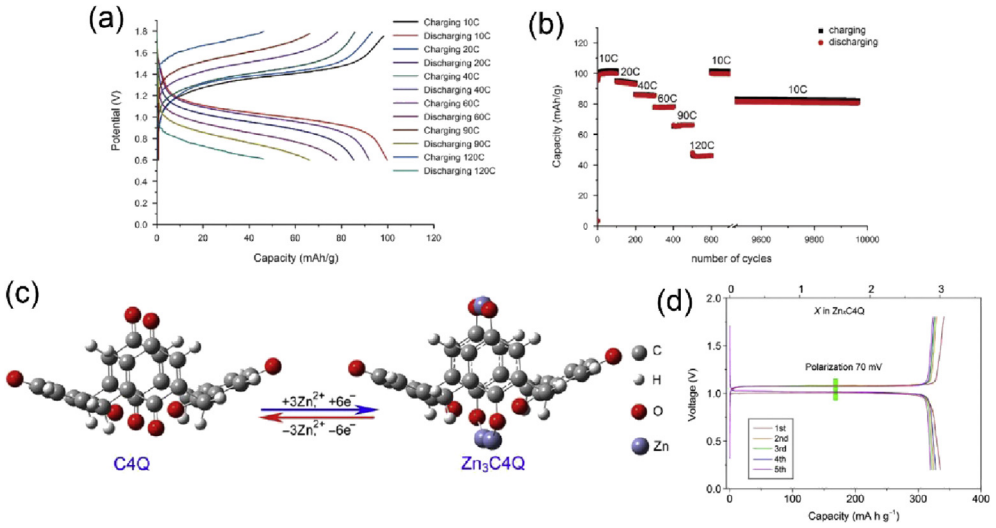

Fig. 10. (a) Charge/discharge curves of the zinc-organic hybrid battery at different charging/discharge speeds of 10, 20, 40, 60, 90, and 120C. (b) The capacity development during extended charge/discharge cycling of a zinc-polymer hybrid battery over 10,000 cycles; the first 600 cycles were at 10, 20, 40, 60,90, and 120C for 100 cycles each, then 9,600 cycles at 10C (the first 100 and the last 500 cycles are displayed) [40]. (c) Optimized configurations of C4Q before and after Zn ion uptake. (d) Galvanostatic discharge/charge curves of Zn/C4Q battery at the current density of 20 mA/g. The upper x-axis represents the uptake number of Zn ions. One Zn^{2+} with two-electron transfers generates a specific capacity of 112 mAh/g^{-1} [39].

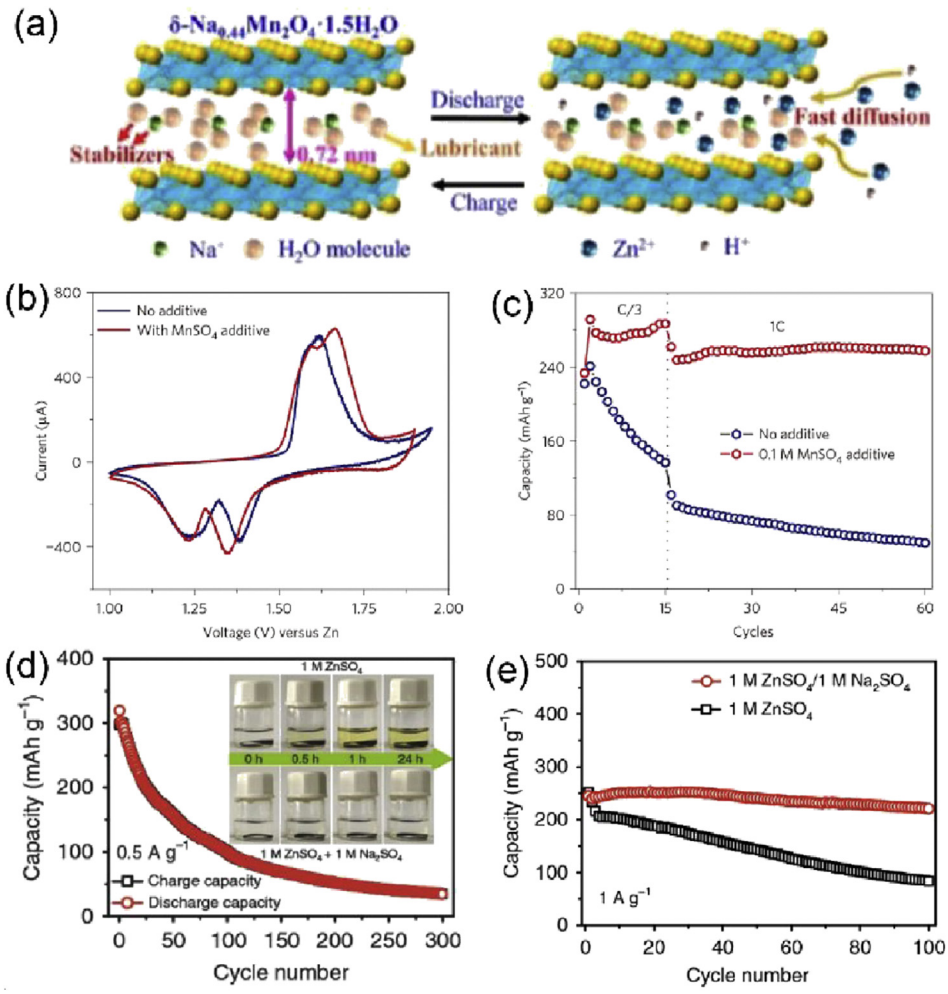

Fig. 11. (a) Schematic illustration of Zn^{2+} insertion/extraction in the as-prepared Na ion and water molecule intercalated layered δ-MnO_2 [91]. (b) Comparison of CV scanning (0.1 mV/s, second cycle) and (c) the cycling performance of MnO_2 electrodes with and without 0.1M $MnSO_4$ additive in a 2M $ZnSO_4$ aqueous electrolyte at C/3 and 1C, respectively [26]. (d) Cycling performance of NVO electrode in $ZnSO_4$ electrolyte. The insets are optical images of NVO electrodes in $ZnSO_4$ and $ZnSO_4/Na_2SO_4$ electrolytes for different periods. (e) Comparison of cycling performance of NVO electrodes at 1 A/g^{-1} in $ZnSO_4$ and $ZnSO_4/Na_2SO_4$ electrolytes [48].

pre-addition of relevant salt also applies to some vanadates. When dipped into $ZnSO_4$ electrolyte, $NaV_3O_8 \cdot 1.5H_2O$ (NVO) would gradually dissolve and the electrolyte would become yellow. Thus, the rapid degradation in capacity with increasing cycle in Zn/$ZnSO_4$/NVO battery is ascribed to the dissolution of NVO electrode. In contrast, $ZnSO_4$ electrolyte would be transparent and colorless after added 1M Na_2SO_4, implying Na_2SO_4 can suppress the dissolution of NVO (Fig. 11d). Thus, the cycling stability of the Zn/NVO battery can be greatly improved by introducing 1M Na_2SO_4 into 1M $ZnSO_4$ electrolyte (Fig. 11e) [48].

4.2.3. Surface coating

The surface coating provides protective layers on the electrode surface, which can buffer volume change and stress caused by ion insertion/extraction and suppress the dissolution of active materials effectively. On one hand, the carbonaceous materials (carbon black, CNTs, graphene, etc.) coating is beneficial to improve the electronic conductivity of cathodes and inhibit dissolution. For instance, the uniform coating of graphene scroll on the α-MnO_2 nanowire increases the electrical conductivity of cathode material and restrains the dissolution of the cathode material during charge/discharge, achieving a prominent capacity of 382.2 mAh/g at 0.3 A/g and excellent long-term cyclic stability with 94% capacity retention after 3,000 cycles at 3 A/g [93]. On the other hand, conductive polymer coating can not only prohibit the dissolution of active materials, but also endow them with flexible characteristics [94,95].

4.2.4. Formation of solid electrolyte interface (SEI) film

SEI film has proved to effectively prevent the dissolution of electrode materials and prohibit the passage of electrons in lithium-ion batteries, enhancing the cyclic stability [96,97]. Similarly, SEI film plays a vital role in maintaining the structural stability of cathode materials in aqueous ZIBs. Recently, Zhou et al. [98] discovered *in situ* electrochemically generated $CaSO_4 \cdot 2H_2O$ SEI film on the Ca_2MnO_4 cathode and unraveled its protective mechanism. The presence of SEI film effectively protects manganese from dissolution, decrease impedance, ameliorate interface, lower activation energy, and facilitate the insertion/extraction of zinc ions, therefore improving cycling stability and prolonging cycle life. As a result, the discharge capacity shows no obvious fluctuation after 1,000 cycles at 1 A/g.

4.3. Introduction of defects

In aqueous ZIBs, the strong electrostatic interaction between divalent Zn^{2+} ions and crystal structures of cathode materials results in sluggish Zn^{2+} ions diffusion and poor electrochemical performance. The issue can be addressed by defect engineering (e.g. cation vacancy, oxygen vacancy, etc.), which is believed to be capable of unlocking the electrochemical activity of viable cathode materials of ZIBs [14,99–101].

Chen et al. [14] introduced cation deficiencies into spinel $ZnMn_2O_4$ to boost insertion of Zn^{2+} ions, as schematically shown in Fig. 12a. In ideal spinel, electrostatic repulsion from Mn cations in a neighboring octahedral site (8d) strongly impedes Zn^{2+} ions migration. The presence of abundant Mn vacancies in $ZnMn_{1.86}Y_{0.14}O_4$ lowers electrostatic barrier of Zn-ion diffusion, allowing for higher mobility of Zn^{2+} ions and consequently faster kinetics (Fig. 12b). The diffusion coefficient of Zn^{2+} in Mn-defected ZMO spinels was determined to be about 0.4×10^{-11} and 1.0×10^{-11} cm^2/s at the charge and discharge plateaus, respectively, which is comparable with Li diffusion coefficient in spinel cathode. The cation-defected $ZnMn_2O_4$ spinel exhibits decent capacity (150 mAh/g at 50 mA/g) and cycling performance (a capacity retention of 94% after 500 cycles at 500 mA/g). Vanadium oxides suffer from strong Coulombic ion–lattice interactions with divalent Zn^{2+}, leading to limited cycling stability. Peng et al. [101] reported an oxygen-deficient V_6O_{13} (O_d-VO) cathode with excellent electrochemical properties, opening up a new avenue for the use of oxygen-deficient cathode materials in ZIBs. Electrochemical performances and simulations demonstrated that introduction of oxygen vacancies into V_6O_{13} lattice can efficiently eliminate strong interactions between Zn^{2+} and the host material (Fig. 12c), favoring fast Zn^{2+} reaction kinetics to achieve high capacities and improved Zn^{2+} pathways for high reversibility (Fig. 12d).

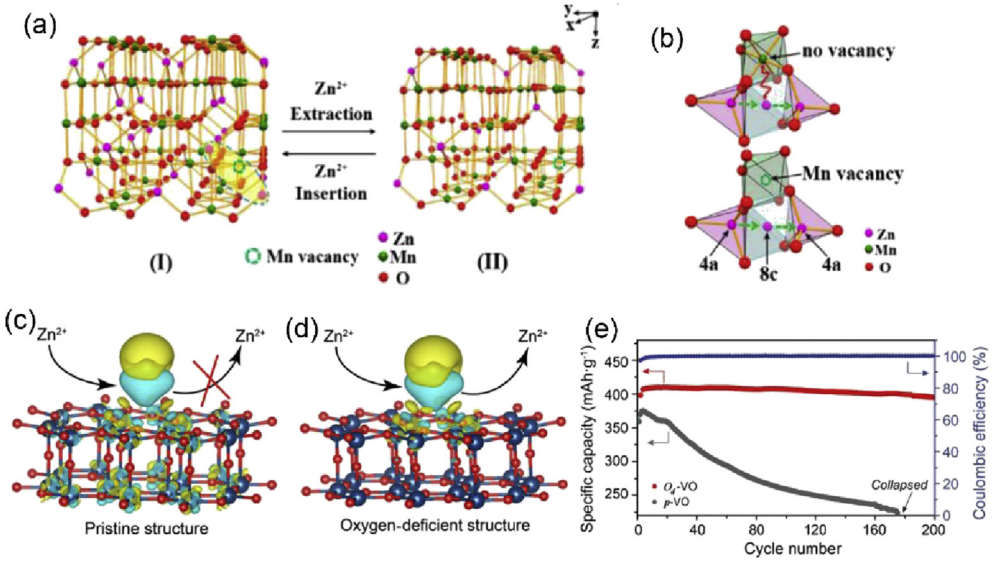

Fig. 12. (a) Schematic illustration of Zn^{2+} insertion/extraction in an extended three-dimensional $ZnMn_2O_4$ spinel framework. (b) Proposed Zn^{2+} diffusion pathway in $ZnMn_2O_4$ spinel without and with Mn vacancies [14]. (c) Illustrations of the Zn^{2+} storage/release for perfect vanadium oxide (p-VO) and O_d-VO, respectively. (d) Comparison of the cycling performance of O_d-VO and p-VO at 200 mA/g^{-1} [101].

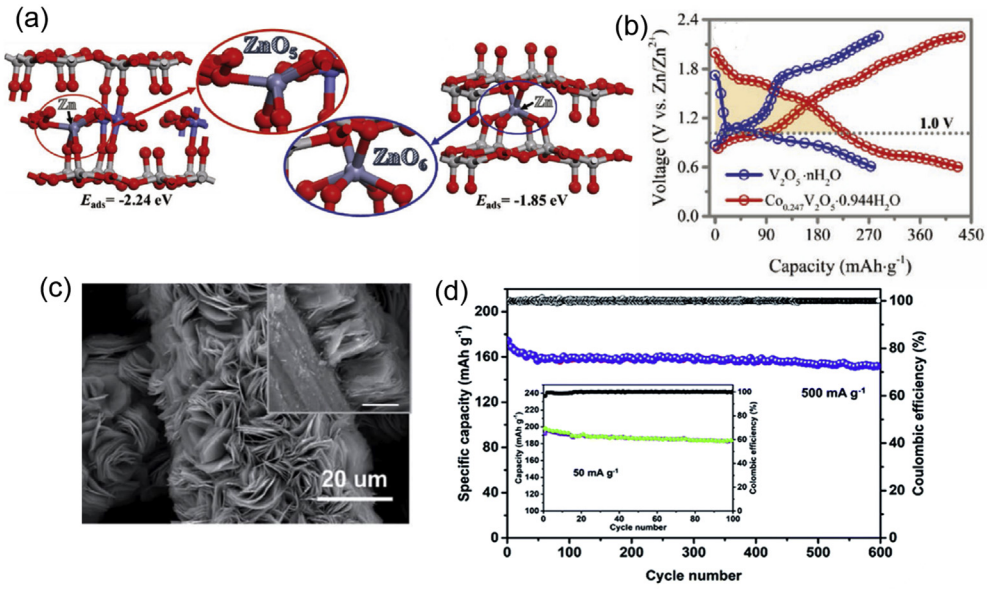

Fig. 13. (a) Galvanostatic charge/discharge curves of $Zn/Co_{0.247}V_2O_5 \cdot 0.944H_2O$ and Zn/V_2O_5 batteries for Zn^{2+} storage comparison. (b) The optimized configuration of Zn-adsorbed $Co_{0.247}V_2O_5 \cdot 0.944H_2O$ and $V_2O_5 \cdot nH_2O$ frameworks, respectively, and their corresponding adsorption energies. The gray spheres represent adsorbed Zn atoms, and Co atoms are depicted by blue spheres [104]. (c) SEM image of the VS_2@SS electrode (inset: cross-section image of VS_2 on SS; the bar is 5 mm). (d) Long-term cycling performances at 500 and 50 mA/g^{-1} (inset) with an areal loading of 11 mg/cm^2 [82].

4.4. Anionic redox exploiting

Most of the aforementioned reactions in the cathode materials are based on conventional cationic redox reaction, whereas anionic redox reactions are demonstrated to contribute to capacity and enhance the operating voltage recently. For example, Chen et al. [102] revealed that anionic (oxygen) redox process occurs at higher voltage (1.75–2.1 V) than the cationic (vanadium) redox (0.8–1.75 V) in $VOPO_4$ cathode, which is conductive to improve operating voltage and energy density. Zhou et al. [103] developed a reversible Zn/VN_xO_y battery operating through simultaneous cationic ($V^{3+} \leftrightarrow V^{2+}$) and anionic ($N^{3-} \leftrightarrow N^{2-}$) redox reaction mechanism, favoring high reversibility and structural stability of VN_xO_y cathode. As a consequence, the battery exhibits fascinating rate capability of 200 mAh/g at 30 A/g along with good cycling stability up to 2,000 cycles.

4.5. Operating voltage enhancement

Besides PBAs (~1.7 V), the operating voltage of other cathode materials is relatively low (~1.3 V for MnO_2, ~0.7 V for $M_xV_nO_m$, and ~1.1 V for organics), leading to the poor energy density of aqueous ZIBs. In this regard, enhancing the operating voltage is crucial to improve the energy density of aqueous ZIBs. The utilization of 'water-in-salt' electrolytes capable of suppressing the electrolysis of water can remarkably extend the operating voltage of ZIBs, enlightening the design of high energy density ZIBs.

For example, the application of a 'water-in-salt' electrolyte (21M LiTFSI +1M $Zn(CF_3SO_3)_2$) in Zn/V_2O_5 aqueous battery, results in the increase of discharge platform from 0.6 to 1.0 V [105]. With 'water-in-salt' electrolyte (20M LiTFSI +1M $Zn(CF_3SO_3)_2$), the 1.7 V high-voltage $Zn/Co_{0.247}V_2O_5 \cdot 0.944H_2O$ battery exhibits an unprecedented high energy density of 458.7 Wh/kg at 0.1 A/g based on the cathode material [104]. Theoretical calculations reveal that the absorption energy of vanadium oxide bronze for Zn^{2+} is remarkably increased with the preintercalation of cobalt ions (Fig. 13a), rendering the high-voltage discharge. The discharge capacity at above 1.0 V reaches 227 mAh/g, accounting for 52.54% of the total capacity (Fig. 13b). The potential drawbacks of 'water-in-salt' include the high cost of the anions (e.g. $TFSI^-$), Li^+, or the electrochemical instability of inexpensive anions, for example, SCN^-, Cl^-, and ClO_4^-.

4.6. Improvement of mass loading for practical application

To date, most cathode materials reported to exhibit promising electrochemical performances were examined at low mass loading (2–3 mg/cm^2). Generally, a typical active material mass loading of ~10 mg/cm^2 is required to meet the requirements of practical implementation. The specific capacity and rate capability significantly decline with increasing mass loading because of the low

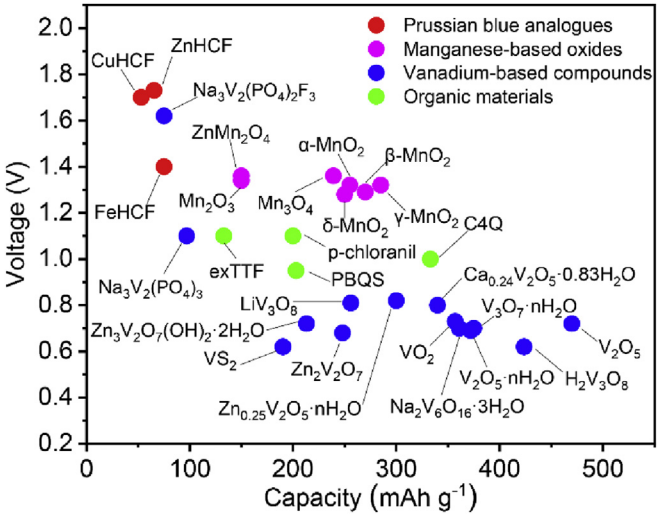

Fig. 14. Average discharge potentials vs. specific capacity of representative cathode materials for ZIBs.

Table 2
Summary of electrochemical performances of various cathode materials for aqueous ZIBs.

Cathode material	Electrolyte	Operating voltage (V)	Specific capacity at x mA/g	Capacity retention after n cycles at y mA/g	Reference
α-MnO_2	1M $ZnSO_4$	1.0–1.9	210 (x = 105)	77% (n = 100, y = 630)	[23]
α-MnO_2	1M $ZnSO_4$	0.8–2.0	205 (x = 10)	66% (n = 30, y = 10)	[55]
α-MnO_2	2M $ZnSO_4$+ 0.1M $MnSO_4$	1.0–1.8	285 (x = 102)	92% (n = 5,000, y = 1,540)	[26]
β-MnO_2	1M $ZnSO_4$	1.0–1.8	180 (x = 200)	75% (n = 200, y = 200)	[56]
β-MnO_2	3M $Zn(CF_3SO_3)_2$ +0.1M $Mn(CF_3SO_3)_2$	0.8–1.9	225 (x = 200)	94% (n = 2,000, y = 2,000)	[44]
λ-MnO_2	1M $ZnSO_4$	–	442.6 (x = 13.8)	–	[46]
δ-MnO_2	1M $ZnSO_4$	1.0–1.8	285 (x = 83)	43% (n = 100, y = 83)	[47]
δ-MnO_2	2M $ZnSO_4$+ 0.1M $MnSO_4$	0.95–1.85	278 (x = 308)	98% (n = 10,000, y = 6,160)	[91]
MnO	2M $ZnSO_4$	1.0–1.9	330 (x = 100)	80.7% (n = 300, y = 300)	[61]
Mn_2O_3	2M $ZnSO_4$+ 0.1M $MnSO_4$	1.0–1.9	148 (x = 100)	65% (n = 2,000, y = 2,000)	[62]
Mn_3O_4	2M $ZnSO_4$	0.8–1.9	239.2 (x = 100)	72% (n = 300, y = 500)	[64]
$ZnMn_2O_4$	3M $Zn(CF_3SO_3)_2$	0.8–2.0	150 (x = 50)	94% (n = 500, y = 500)	[14]
V_2O_5	3M $ZnSO_4$	0.4–1.4	224 (x = 100)	67% (n = 400, y = 1,000)	[67]
V_2O_5	3M $Zn(CF_3SO_3)_2$	0.2–1.6	470 (x = 200)	91.1% (n = 4,000, y = 5,000)	[34]
$V_2O_5 \cdot nH_2O$/Graphene	3M $Zn(CF_3SO_3)_2$	0.2–1.6	381 (x = 60)	71% (n = 900, y = 6,000)	[38]
$V_3O_7 \cdot H_2O$	1M $ZnSO_4$	0.4–1.1	375 (x = 375)	80% (n = 200, y = 3,000)	[65]
$H_2V_3O_8$	3M $Zn(CF_3SO_3)_2$	0.2–1.6	423 (x = 100)	94.3% (n = 1,000, y = 5,000)	[68]
VO_2	3M $Zn(CF_3SO_3)_2$	0.3–1.5	357 (x = 100)	91.2% (n = 300, y = 2,000)	[66]
VO_2	3M $Zn(CF_3SO_3)_2$	0.7–1.7	274 (x = 100)	79% (n = 10,000, y = 10,000)	[70]
$Zn_{0.3}V_2O_5 \cdot 1.5H_2O$	3M $Zn(CF_3SO_3)_2$	0.3–1.6	426 (x = 200)	96% (n = 20,000, y = 10,000)	[63]
$Zn_{0.25}V_2O_5 \cdot nH_2O$	1M $ZnSO_4$	0.5–1.4	300 (x = 50)	80% (n = 1,000, y = 2,400)	[8]
$LixV_2O_5 \cdot nH_2O$	2M $ZnSO_4$	0.4–1.4	470 (x = 500)	63% (n = 1,000, y = 10,000)	[74]
$Ca_{0.24}V_2O_5 \cdot 0.83H_2O$	1M $ZnSO_4$	0.6–1.6	340 (x = 68)	96% (n = 3,000, y = 27,200)	[36]
LiV_3O_8	1M $ZnSO_4$	0.6–1.2	280 (x = 16)	75% (n = 65, y = 133)	[71]
$NaV_3O_8 \cdot 1.5H_2O$	1M $ZnSO_4$ + 1M Na_2SO_4	0.3–1.25	380 (x = 50)	82% (n = 1,000, y = 4,000)	[48]
$Na_2V_6O_{16} \cdot 1.63H_2O$	3M $Zn(CF_3SO_3)_2$	0.2–1.6	353 (x = 50)	90% (n = 6,000, y = 5,000)	[72]
$Na_2V_6O_{16} \cdot 3H_2O$	1M $ZnSO_4$	0.4–1.4	361 (x = 101)	84.5% (n = 1,000, y = 14,440)	[37]
$Zn_3V_2O_7(OH)_2 \cdot 2H_2O$	1M $ZnSO_4$	0.2–1.8	213 (x = 50)	68% (n = 300, y = 200)	[73]
$Zn_2V_2O_7$	1M $ZnSO_4$	0.4–1.4	248 (x = 50)	85% (n = 1,000, y = 4,000)	[79]
VS_2	1M $ZnSO_4$	0.4–1.4	190 (x = 50)	98% (n = 200, y = 50)	[33]
$Na_3V_2(PO_4)_3$/C	0.5M $Zn(CH_3COO)_2$	0.8–1.7	92 (x = 50)	74% (n = 200, y = 50)	[32]
$Na_3V_2(PO_4)_2F_3$	2M $Zn(CF_3SO_3)_2$	0.8–1.9	61.7 (x = 20)	95% (n = 4,000, y = 1,000)	[81]
CuHCF	0.02M $ZnSO_4$	0.45–1.4	53 (x = 60)	96% (n = 100, y = 60)	[30]
ZnHCF	1M $ZnSO_4$	0.8–1.9	65.4 (x = 60)	81% (n = 100, y = 300)	[29]
FeHCF	21M LiTFSI+ 1M Zn $(TFSI)_2$	0.01–2.3	76 (x = 1,000)	73% (n = 10,000, y = 3,000)	[84]
exTTF	1M Zinc tetrafluoroborate	0.6–1.7	133 (x = 2,660)	86% (n = 10,000, y = 159,600)	[40]
quinone (C4Q)	3M $Zn(CF_3SO_3)_2$	0.2–1.8	335 (x = 20)	87% (n = 1,000, y = 500)	[39]

electrical conductivity and limited ion diffusion. Thus, it is very critical, and certainly very challenging, but somewhat ignored in literature, to improve the electrochemical performance of cathode materials at commercial levels of mass loading (~10 mg/cm^2). Recently, some researchers have started to focus on the issue of mass loading and make advances in enhancing the electrochemical properties of cathode materials at high mass loading [82,83,106].

For example, Zhang et al. [82] designed hierarchical 1T VS_2 nanoflowers grown directly on an SS mesh as cathode of ZIBs (Fig. 13c). The open structure with a high electrical conductivity provides abundant contact area with the electrolyte, facilitating electron and ion transport. As a consequence, the VS_2 @SS electrode with a mass loading of 11 mg/cm^2 exhibits a discharge capacity of 174 mAh/g at 500 mA/g and good cycling stability with 90% capacity retention after 600 cycles (Fig. 13d), suggesting its potential for practical applications.

5. Summary and outlook

In this review, recent advances in cathode materials of aqueous ZIBs are briefed. To date, various cathode materials have been investigated for ZIBs, which can be classified into the following four main families: PBAs, manganese oxides, vanadium-based compounds, and organics. The unique compositions, crystal structures, and morphologies endow these cathode materials with different electrode reaction mechanisms and electrochemical performances. The electrode reactions in cathodes involve reversible Zn^{2+} insertion/extraction, chemical conversion reactions, and reversible Zn^{2+} and H^+ co-insertion/extraction mechanisms. The electrochemical properties of four types of cathode materials are summarized in Fig. 14 and Table 2. PBAs exhibit high operating voltage (~1.7 V) but limited specific capacities (<80 mAh/g). Manganese oxides and organics display higher specific capacities and moderate discharge voltages, rate capabilities, and cycling performance. In contrast, vanadium-based compounds with low discharge plateaus ~0.7 V show decent rate and cycling performances. Each type of cathode material has particular merits and drawbacks, rendering unsatisfactory comprehensive electrochemical properties. In this regard, some effective strategies have been adopted to address the issues encountered, such as preintercalation of guests as pillars and electrolyte optimization to stabilize the host structure, introduction of defects and nanostructure regulating to promote reaction kinetics, and so on. Finally, performances with high mass loading at the practical level are far worse than those normally made in the laboratory with low mass loads. New strategies are indispensable to solve the low electrical conductivity and limited ion diffusion associated with high mass loading.

Declaration of Competing Interest

The authors declare that they have no known competing financial interests or personal relationships that could have appeared to influence the work reported in this paper.

Acknowledgments

The authors acknowledge financial support from the National Science Foundation of China (NSFC-21673004, 21627805, and 21821004) and MOST (2017YFA0204702) China.

References

[1] M. Armand, J.M. Tarascon, Building better batteries, Nature 451 (2008) 652–657.
[2] B. Dunn, H. Kamath, J.-M. Tarascon, Electrical energy storage for the grid: a battery of choices, Science 334 (2011) 928–935.
[3] J.M. Tarascon, M. Armand, Issues and challenges facing rechargeable lithium batteries, Nature 414 (2001) 359–367.
[4] Y. Lu, J.B. Goodenough, Y. Kim, Aqueous cathode for next-generation alkali-ion batteries, J. Am. Chem. Soc. 133 (2011) 5756–5759.
[5] D. Larcher, J.M. Tarascon, Towards greener and more sustainable batteries for electrical energy storage, Nat. Chem. 7 (2015) 19–29.
[6] J.B. Goodenough, Y. Kim, Challenges for rechargeable Li batteries, Chem. Mater. 22 (2010) 587–603.
[7] J.B. Goodenough, K.S. Park, The Li-ion rechargeable battery: a perspective, J. Am. Chem. Soc. 135 (2013) 1167–1176.
[8] D. Kundu, B.D. Adams, V. Duffort, S.H. Vajargah, L.F. Nazar, A high-capacity and long-life aqueous rechargeable zinc battery using a metal oxide intercalation cathode, Nat. Energy 1 (2016) 16119.
[9] J.Y. Luo, Y.Y. Xia, Aqueous lithium-ion battery $LiTi_2(PO_4)_3/LiMn_2O_4$ with high power and energy densities as well as superior cycling stability, Adv. Funct. Mater. 17 (2007) 3877–3884.
[10] D. Su, A. McDonagh, S.-Z. Qiao, G. Wang, High-capacity aqueous potassium-ion batteries for large-scale energy storage, Adv. Mater. 29 (2017) 1604007.
[11] X.Y. Wu, Y. Luo, M.Y. Sun, J.F. Qian, Y.L. Cao, X.P. Ai, H.X. Yang, Low-defect prussian blue nanocubes as high capacity and long life cathodes for aqueous Na-ion batteries, Nano Energy 13 (2015) 117–123.
[12] K.W. Nam, S. Kim, S. Lee, M. Salama, I. Shterenberg, Y. Gofer, J.S. Kim, E. Yang, C.S. Park, J.S. Kim, S.S. Lee, W.S. Chang, S.G. Doo, Y.N. Jo, Y. Jung, D. Aurbach, J.W. Choi, The high performance of crystal water containing manganese birnessite cathodes for magnesium batteries, Nano Lett. 15 (2015) 4071–4079.
[13] S. Liu, J.J. Hu, N.F. Yan, G.L. Pan, G.R. Li, X.P. Gao, Aluminum storage behavior of anatase TiO_2 nanotube arrays in aqueous solution for aluminum ion batteries, Energy Environ. Sci. 5 (2012) 9743.
[14] N. Zhang, F. Cheng, Y. Liu, Q. Zhao, K. Lei, C. Chen, X. Liu, J. Chen, Cation-deficient spinel $ZnMn_2O_4$ cathode in $Zn(CF_3SO_3)_2$ electrolyte for rechargeable aqueous Zn-ion battery, J. Am. Chem. Soc. 138 (2016) 12894–12901.
[15] J.F. Parker, C.N. Chervin, I.R. Pala, M. Machler, M.F. Burz, J.W. Long, D.R. Rolison, Rechargeable nickel-3D zinc batteries: an energy-dense, safer alternative to lithium-ion, Science 356 (2017) 414–417.
[16] Z. Liu, J. Wang, H. Ding, S. Chen, X. Yu, B. Lu, Carbon nanoscrolls for aluminum battery, ACS Nano 12 (2018) 8456–8466.
[17] Z. Liu, J. Wang, X. Jia, W. Li, Q. Zhang, L. Fan, H. Ding, H. Yang, X. Yu, X. Li, B. Lu, Graphene armored with a crystal carbon shell for ultrahigh-performance potassium ion batteries and aluminum batteries, ACS Nano 13 (2019) 10631–10642.
[18] G.A. Elia, K. Marquardt, K. Hoeppner, S. Fantini, R. Lin, E. Knipping, W. Peters, J.-F. Drillet, S. Passerini, R. Hahn, An overview and future perspectives of aluminum batteries, Adv. Mater. 28 (2016) 7564–7579.
[19] H. Zhang, K. Ye, K. Zhu, R. Cang, J. Yan, K. Cheng, G. Wang, D. Cao, High-energy-density aqueous magnesium-ion battery based on a carbon-coated $FeVO_4$ anode and a Mg-OMS-1 cathode, Chem.-Eur. J. 23 (2017) 17118–17126.
[20] F. Ambroz, T.J. Macdonald, T. Nann, Trends in aluminium-based intercalation batteries, Adv. Energy Mater. 7 (2017).
[21] X. Sun, P. Bonnick, L.F. Nazar, Layered TiS_2 positive electrode for Mg batteries, ACS Energy Lett. 1 (2016) 297–301.
[22] X.G. Zhang, Corrosion and electrochemistry of zinc, Br. Corrosion J. 32 (1996) 28–29.
[23] C. Xu, B. Li, H. Du, F. Kang, Energetic zinc ion chemistry: the rechargeable zinc ion battery, Angew. Chem. Int. Ed. 51 (2012) 933–935.
[24] T. Yamamoto, T. Shoji, Rechargeable $Zn/ZnSO_4/MnO_2$-type cells, Inorg. Chim. Acta. 117 (1986) L27–L28.
[25] D.E. Turney, J.W. Gallaway, G.G. Yadav, R. Ramirez, M. Nyce, S. Banerjee, Y.-c. K. Chen-Wiegart, J. Wang, M.J. D'Ambrose, S. Kolhekar, J. Huang, X. Wei, Rechargeable zinc alkaline anodes for long-cycle energy storage, Chem. Mater. 29 (2017) 4819–4832.
[26] H. Pan, Y. Shao, P. Yan, Y. Cheng, K.S. Han, Z. Nie, C. Wang, J. Yang, X. Li, P. Bhattacharya, K.T. Mueller, J. Liu, Reversible aqueous zinc/manganese oxide energy storage from conversion reactions, Nat. Energy 1 (2016) 16039.
[27] Z. Liu, P. Bertram, F. Endres, Bio-degradable zinc-ion battery based on a prussian blue analogue cathode and a bio-ionic liquid-based electrolyte, J. Solid State Electrochem. 21 (2017) 2021–2027.
[28] Z. Liu, G. Pulletikurthi, F. Endres, A prussian blue/zinc secondary battery with a bio-ionic liquid-water mixture as electrolyte, ACS Appl. Mater. Interfaces 8 (2016) 12158–12164.
[29] L. Zhang, L. Chen, X. Zhou, Z. Liu, Towards high-voltage aqueous metal-ion batteries beyond 1.5 V: the zinc/zinc hexacyanoferrate system, Adv. Energy Mater. 5 (2015) 1400930.
[30] R. Trocoli, F. La Mantia, An aqueous zinc-ion battery based on copper hexacyanoferrate, ChemSusChem 8 (2015) 481–485.
[31] W. Sun, F. Wang, S. Hou, C. Yang, X. Fan, Z. Ma, T. Gao, F. Han, R. Hu, M. Zhu, C. Wang, Zn/MnO_2 battery chemistry with H^+ and Zn^{2+} coinsertion, J. Am. Chem. Soc. 139 (2017) 9775–9778.
[32] G. Li, Z. Yang, Y. Jiang, C. Jin, W. Huang, X. Ding, Y. Huang, Towards polyvalent ion batteries: a zinc-ion battery based on nasicon structured $Na_3V_2(PO_4)_3$, Nano Energy 25 (2016) 211–217.
[33] P. He, M. Yan, G. Zhang, R. Sun, L. Chen, Q. An, L. Mai, Layered VS_2 nanosheet-based aqueous Zn ion battery cathode, Adv. Energy Mater. 7 (2017) 1601920.
[34] N. Zhang, Y. Dong, M. Jia, X. Bian, Y. Wang, M. Qiu, J. Xu, Y. Liu, L. Jiao, F. Cheng, Rechargeable aqueous $Zn–V_2O_5$ battery with high energy density and long cycle life, ACS Energy Lett. 3 (2018) 1366–1372.
[35] S. Guo, G. Fang, S. Liang, M. Chen, X. Wu, J. Zhou, Structural perspective on revealing energy storage behaviors of silver vanadate cathodes in aqueous zinc-ion batteries, Acta Mater. 180 (2019) 51–59.
[36] C. Xia, J. Guo, P. Li, X. Zhang, H.N. Alshareef, Highly stable aqueous zinc-ion storage using a layered calcium vanadium oxide bronze cathode, Angew. Chem. Int. Ed. 57 (2018) 3943–3948.
[37] V. Soundharrajan, B. Sambandam, S. Kim, M.H. Alfaruqi, D.Y. Putro, J. Jo, S. Kim, V. Mathew, Y.K. Sun, J. Kim, $Na_2V_6O_{16}\cdot 3H_2O$ barnesite nanorod: an open door to display a stable and high energy for aqueous rechargeable Zn-ion batteries as cathodes, Nano Lett. 18 (2018) 2402–2410.
[38] M. Yan, P. He, Y. Chen, S. Wang, Q. Wei, K. Zhao, X. Xu, Q. An, Y. Shuang, Y. Shao, K.T. Mueller, L. Mai, J. Liu, J. Yang, Water-lubricated intercalation in $V_2O_5.nH_2O$ for high-capacity and high-rate aqueous rechargeable zinc batteries, Adv. Mater. 30 (2018).
[39] Q. Zhao, W. Huang, Z. Luo, L. Liu, Y. Lu, Y. Li, L. Li, J. Hu, H. Ma, J. Chen, High-capacity aqueous zinc batteries using sustainable quinone electrodes, Sci. Adv. 4 (2018).
[40] B. Häupler, C. Rössel, A.M. Schwenke, J. Winsberg, D. Schmidt, A. Wild, U.S. Schubert, Aqueous zinc-organic polymer battery with a high rate performance and long lifetime, NPG Asia Mater. 8 (2016) e283-e283.
[41] Y. Marcus, Ionic-radii in aqueous-solutions, Chem. Rev. 88 (1988) 1475–1498.
[42] E.R. Nightingale, Phenomenological theory of ion solvation - effective radii of hydrated ions, J. Phys. Chem. 63 (1959) 1381–1387.
[43] A. Konarov, N. Voronina, J.H. Jo, Z. Bakenov, Y.K. Sun, S.T. Myung, Present and future perspective on electrode materials for rechargeable zinc-ion batteries, ACS Energy Lett. 3 (2018) 2620–2640.
[44] N. Zhang, F. Cheng, J. Liu, L. Wang, X. Long, X. Liu, F. Li, J. Chen, Rechargeable aqueous zinc-manganese dioxide batteries with high energy and power densities, Nat. Commun. 8 (2017) 405.
[45] M.H. Alfaruqi, V. Mathew, J. Gim, S. Kim, J. Song, J.P. Baboo, S.H. Choi, J. Kim, Electrochemically induced structural transformation in a γ-MnO_2 cathode of a high capacity zinc-ion battery system, Chem. Mater. 27 (2015) 3609–3620.
[46] C. Yuan, Y. Zhang, Y. Pan, X. Liu, G. Wang, D. Cao, Investigation of the intercalation of polyvalent cations (Mg^{2+}, Zn^{2+}) into λ-MnO_2 for rechargeable aqueous battery, Electrochim. Acta 116 (2014) 404–412.
[47] M.H. Alfaruqi, J. Gim, S. Kim, J. Song, D.T. Pham, J. Jo, Z. Xiu, V. Mathew, J. Kim, A layered δ-MnO_2 nanoflake cathode with high zinc-storage capacities for eco-friendly battery applications, Electrochem, Commun. Now. 60 (2015) 121–125.
[48] F. Wan, L. Zhang, X. Dai, X. Wang, Z. Niu, J. Chen, Aqueous rechargeable zinc/sodium vanadate batteries with enhanced performance from simultaneous insertion of dual carriers, Nat. Commun. 9 (2018) 1656.
[49] C. Xie, T. Li, C. Deng, Y. Song, H. Zhang, X. Li, A highly reversible neutral zinc/manganese battery for stationary energy storage, Energy Environ. Sci. 13 (2020) 135–143.
[50] G. Liang, F. Mo, H. Li, Z. Tang, Z. Liu, D. Wang, Q. Yang, L. Ma, C. Zhi, A universal principle to design reversible aqueous batteries based on deposition–dissolution mechanism, Adv. Energy Mater. 9 (2019) 1901838.
[51] D. Chao, W. Zhou, C. Ye, Q. Zhang, Y. Chen, L. Gu, K. Davey, S.Z. Qiao, An electrolytic Zn-MnO_2 battery for high-voltage and scalable energy storage, Angew. Chem. Int. Ed. 58 (2019) 7823–7828.
[52] W. Chen, G. Li, A. Pei, Y. Li, L. Liao, H. Wang, J. Wan, Z. Liang, G. Chen, H. Zhang, J. Wang, Y. Cui, A manganese–hydrogen battery with potential for grid-scale energy storage, Nat. Energy 3 (2018) 428.
[53] X. Guo, J. Zhou, C. Bai, X. Li, G. Fang, S. Liang, Zn/MnO_2 battery chemistry with dissolution-deposition mechanism, Mater. Today Energy 16 (2020) 100396.
[54] G. Li, W. Chen, H. Zhang, Y. Gong, F. Shi, J. Wang, R. Zhang, G. Chen, Y. Jin, T. Wu, Z. Tang, Y. Cui, Membrane-free Zn/MnO_2 flow battery for large-scale energy storage, Adv. Energy Mater. 10 (2020).

[55] B. Lee, C.S. Yoon, H.R. Lee, K.Y. Chung, B.W. Cho, S.H. Oh, Electrochemically-induced reversible transition from the tunneled to layered polymorphs of manganese dioxide, Sci. Rep. 4 (2014) 6066.

[56] S. Islam, M.H. Alfaruqi, V. Mathew, J. Song, S. Kim, S. Kim, J. Jo, J.P. Baboo, D.T. Pham, D.Y. Putro, Y.-K. Sun, J. Kim, Facile synthesis and the exploration of the zinc storage mechanism of β-MnO_2 nanorods with exposed (101) planes as a novel cathode material for high performance eco-friendly zinc-ion batteries, J. Mater. Chem. A 5 (2017) 23299–23309.

[57] C. Wei, C. Xu, B. Li, H. Du, F. Kang, Preparation and characterization of manganese dioxides with nano-sized tunnel structures for zinc ion storage, J. Phys. Chem. Solid. 73 (2012) 1487–1491.

[58] G. Kumar, Electrochemical characterization of poly(vinylidenefluoride)-zinc triflate gel polymer electrolyte and its application in solid-state zinc batteries, Solid State Ionics 160 (2003) 289–300.

[59] J. Luo, Q.H. Zhang, A.M. Huang, O. Giraldo, S.L. Suib, Double-aging method for preparation of stabilized Na-buserite and transformations to todorokites incorporated with various metals, Inorg. Chem. 38 (1999) 6106–6113.

[60] Z. Sun, D. Shu, H. Chen, C. He, S. Tang, J. Zhang, Microstructure and supercapacitive properties of buserite-type manganese oxide with a large basal spacing, J. Power Sources 216 (2012) 425–433.

[61] J. Wang, J.-G. Wang, H. Liu, Z. You, C. Wei, F. Kang, Electrochemical activation of commercial MnO microsized particles for high-performance aqueous zinc-ion batteries, J. Power Sources 438 (2019) 226951–226957.

[62] B. Jiang, C. Xu, C. Wu, L. Dong, J. Li, F. Kang, Manganese sesquioxide as cathode material for multivalent zinc ion battery with high capacity and long cycle life, Electrochim. Acta 229 (2017) 422–428.

[63] L. Wang, X. Cao, L. Xu, J. Chen, J. Zheng, Transformed akhtenskite MnO_2 from Mn_3O_4 as cathode for a rechargeable aqueous zinc ion battery, ACS Sustain. Chem. Eng. 6 (2018) 16055–16063.

[64] J. Hao, J. Mou, J. Zhang, L. Dong, W. Liu, C. Xu, F. Kang, Electrochemically induced spinel-layered phase transition of Mn_3O_4 in high performance neutral aqueous rechargeable zinc battery, Electrochim. Acta 259 (2018) 170–178.

[65] D. Kundu, S. Hosseini Vajargah, L. Wan, B. Adams, D. Prendergast, L.F. Nazar, Aqueous vs. nonaqueous Zn-ion batteries: consequences of the desolvation penalty at the interface, Energy Environ. Sci. 11 (2018) 881–892.

[66] J. Ding, Z. Du, L. Gu, B. Li, L. Wang, S. Wang, Y. Gong, S. Yang, Ultrafast Zn^{2+} intercalation and deintercalation in vanadium dioxide, Adv. Mater. 30 (2018), e1800762.

[67] J. Zhou, L. Shan, Z. Wu, X. Guo, G. Fang, S. Liang, Investigation of V_2O_5 as a low-cost rechargeable aqueous zinc ion battery cathode, Chem. Commun. 54 (2018) 4457–4460.

[68] P. He, Y. Quan, X. Xu, M. Yan, W. Yang, Q. An, L. He, L. Mai, High-performance aqueous zinc-ion battery based on layered $H_2V_3O_8$ nanowire cathode, Small 13 (2017) 1702551.

[69] P. Wang, X. Shi, Z. Wu, S. Guo, J. Zhou, S. Liang, Layered hydrated vanadium oxide as highly reversible intercalation cathode for aqueous Zn-ion batteries, Carbon Energy (2020) 1–8.

[70] T. Wei, Q. Li, G. Yang, C. Wang, An electrochemically induced bilayered structure facilitates long-life zinc storage of vanadium dioxide, J. Mater. Chem. A 6 (2018) 8006–8012.

[71] M.H. Alfaruqi, V. Mathew, J. Song, S. Kim, S. Islam, D.T. Pham, J. Jo, S. Kim, J.P. Baboo, Z. Xiu, K.-S. Lee, Y.-K. Sun, J. Kim, Electrochemical zinc intercalation in lithium vanadium oxide: a high-capacity zinc-ion battery cathode, Chem. Mater. 29 (2017) 1684–1694.

[72] P. Hu, T. Zhu, X. Wang, X. Wei, M. Yan, J. Li, W. Luo, W. Yang, W. Zhang, L. Zhou, Z. Zhou, L. Mai, Highly durable $Na_2V_6O_{16}.1.63H_2O$ nanowire cathode for aqueous zinc-ion battery, Nano Lett. 18 (2018) 1758–1763.

[73] C. Xia, J. Guo, Y. Lei, H. Liang, C. Zhao, H.N. Alshareef, Rechargeable aqueous zinc-ion battery based on porous framework zinc pyrovanadate intercalation cathode, Adv. Mater. 30 (2018) 1705580.

[74] Y. Yang, Y. Tang, G. Fang, L. Shan, J. Guo, W. Zhang, C. Wang, L. Wang, J. Zhou, S. Liang, Li^+ intercalated $V_2O_5 \cdot nH_2O$ with enlarged layer spacing and fast ion diffusion as an aqueous zinc-ion battery cathode, Energy Environ. Sci. 11 (2018) 3157–3162.

[75] P. He, G. Zhang, X. Liao, M. Yan, X. Xu, Q. An, J. Liu, L. Mai, Sodium ion stabilized vanadium oxide nanowire cathode for high-performance zinc-ion batteries, Adv. Energy Mater. 8 (2018) 1702463.

[76] F. Ming, H. Liang, Y. Lei, S. Kandambeth, M. Eddaoudi, H.N. Alshareef, Layered $MgxV_2O_5 \cdot nH_2O$ as cathode material for high-performance aqueous zinc ion batteries, ACS Energy Lett. 3 (2018) 2602–2609.

[77] C. Liu, Z. Neale, J. Zheng, X. Jia, J. Huang, M. Yan, M. Tian, M. Wang, J. Yang, G. Cao, Expanded hydrated vanadate for high-performance aqueous zinc-ion batteries, Energy Environ. Sci. 12 (2019) 2273–2285.

[78] L. Wang, K.-W. Huang, J. Chen, J. Zheng, Ultralong cycle stability of aqueous zinc-ion batteries with zinc vanadium oxide cathodes, Sci. Adv. 5 (2019), eeax4279.

[79] B. Sambandam, V. Soundharrajan, S. Kim, M.H. Alfaruqi, J. Jo, S. Kim, V. Mathew, Y.-k. Sun, J. Kim, Aqueous rechargeable Zn-ion batteries: an imperishable and high-energy $Zn_2V_2O_7$ nanowire cathode through intercalation regulation, J. Mater. Chem. A 6 (2018) 3850–3856.

[80] H. Qin, Z. Yang, L. Chen, X. Chen, L. Wang, A high-rate aqueous rechargeable zinc ion battery based on the VS_4@rGO nanocomposite, J. Mater. Chem. A 6 (2018) 23757–23765.

[81] W. Li, K. Wang, S. Cheng, K. Jiang, A long-life aqueous Zn-ion battery based on $Na_3V_2(PO_4)_2F_3$ cathode, Energy Stor. Mater. 15 (2018) 14–21.

[82] T. Jiao, Q. Yang, S. Wu, Z. Wang, D. Chen, D. Shen, B. Liu, J. Cheng, H. Li, L. Ma, C. Zhi, W. Zhang, Binder-free hierarchical VS_2 electrodes for high-performance aqueous Zn ion batteries towards commercial level mass loading, J. Mater. Chem. A 7 (2019) 16330–16338.

[83] F. Wang, E. Hu, W. Sun, T. Gao, X. Ji, X. Fan, F. Han, X.-Q. Yang, K. Xu, C. Wang, A rechargeable aqueous Zn^{2+}-battery with high power density and a long cycle-life, Energy Environ. Sci. 11 (2018) 3168–3175.

[84] Q. Yang, F. Mo, Z. Liu, L. Ma, X. Li, D. Fang, S. Chen, S. Zhang, C. Zhi, Activating c-coordinated iron of iron hexacyanoferrate for Zn hybrid-ion batteries with 10 000-cycle lifespan and superior rate capability, Adv. Mater. 31 (2019), e1901521.

[85] Y. Ma, X. Xie, R. Lv, B. Na, J. Ouyang, H. Liu, Nanostructured polyaniline–cellulose papers for solid-state flexible aqueous Zn-ion battery, ACS Sustain. Chem. Eng. 6 (2018) 8697–8703.

[86] H.-Y. Shi, Y.-J. Ye, K. Liu, Y. Song, X. Sun, A long-cycle-life self-doped polyaniline cathode for rechargeable aqueous zinc batteries, Angew. Chem. Int. Ed. 57 (2018) 16359–16363.

[87] G. Dawut, Y. Lu, L. Miao, J. Chen, High-performance rechargeable aqueous Zn-ion batteries with a poly(benzoquinonyl sulfide) cathode, Inorg. Chem. Front. 5 (2018) 1391–1396.

[88] D. Kundu, P. Oberholzer, C. Glaros, A. Bouzid, E. Tervoort, A. Pasquarello, M. Niederberger, Organic cathode for aqueous Zn-ion batteries: taming a unique phase evolution toward stable electrochemical cycling, Chem. Mater. 30 (2018) 3874–3881.

[89] X. Yu, A. Manthiram, Electrochemical energy storage with an aqueous zinc–quinone chemistry enabled by a mediator-ion solid electrolyte, ACS Appl. Energy Mater. 1 (2018) 273–277.

[90] Y. Fang, X.-Y. Yu, X.W. Lou, Nanostructured electrode materials for advanced sodium-ion batteries, Matter 1 (2019) 90–114.

[91] D. Wang, L. Wang, G. Liang, H. Li, Z. Liu, Z. Tang, J. Liang, C. Zhi, A superior delta-MnO_2 cathode and a self-healing Zn-delta-MnO_2 battery, ACS Nano 13 (2019) 10643–10652.

[92] J. Huang, Z. Wang, M. Hou, X. Dong, Y. Liu, Y. Wang, Y. Xia, Polyaniline-intercalated manganese dioxide nanolayers as a high-performance cathode material for an aqueous zinc-ion battery, Nat. Commun. 9 (2018) 2906.

[93] B. Wu, G. Zhang, M. Yan, T. Xiong, P. He, L. He, X. Xu, L. Mai, Graphene scroll-coated alpha-MnO_2 nanowires as high-performance cathode materials for aqueous Zn-ion battery, Small 14 (2018), e1703850.

[94] D. Xu, H. Wang, F. Li, Z. Guan, R. Wang, B. He, Y. Gong, X. Hu, Conformal conducting polymer shells on V_2O_5 nanosheet arrays as a high-rate and stable zinc-ion battery cathode, Adv. Mater. Interfaces 6 (2019) 1801506.

[95] H. Zhang, J. Wang, Q. Liu, W. He, Z. Lai, X. Zhang, M. Yu, Y. Tong, X. Lu, Extracting oxygen anions from $ZnMn_2O_4$: robust cathode for flexible all-solid-state Zn-ion batteries, Energy Stor. Mater. 21 (2019) 154–161.

[96] L. Suo, D. Oh, Y. Lin, Z. Zhuo, O. Borodin, T. Gao, F. Wang, A. Kushima, Z. Wang, H.C. Kim, Y. Qi, W. Yang, F. Pan, J. Li, K. Xu, C. Wang, How solid-electrolyte interphase forms in aqueous electrolytes, J. Am. Chem. Soc. 139 (2017) 18670–18680.

[97] J. Zhi, A.Z. Yazdi, G. Valappil, J. Haime, P. Chen, Artificial solid electrolyte interphase for aqueous lithium energy storage systems, Sci. Adv. 3 (2017), e1701010.

[98] S. Guo, S. Liang, B. Zhang, G. Fang, D. Ma, J. Zhou, Cathode interfacial layer formation via in situ electrochemically charging in aqueous zinc-ion battery, ACS Nano 13 (2019) 13456–13464.

[99] M. Han, J. Huang, S. Liang, L. Shan, X. Xie, Z. Yi, Y. Wang, S. Guo, J. Zhou, Oxygen defects in beta-MnO_2 enabling high-performance rechargeable aqueous zinc/manganese dioxide battery, iScience 23 (2020) 100797.

[100] C. Zhu, G. Fang, S. Liang, Z. Chen, Z. Wang, J. Ma, H. Wang, B. Tang, X. Zheng, J. Zhou, Electrochemically induced cationic defect in MnO intercalation cathode for aqueous zinc-ion battery, Energy Stor. Mater. 24 (2020) 394–401.

[101] M. Liao, J. Wang, L. Ye, H. Sun, Y. Wen, C. Wang, X. Sun, B. Wang, H. Peng, A deep-cycle aqueous zinc-ion battery containing an oxygen-deficient vanadium oxide cathode, Angew. Chem. Int. Ed. 59 (2020) 2273–2278.

[102] F. Wan, Y. Zhang, L. Zhang, D. Liu, C. Wang, L. Song, Z. Niu, J. Chen, Reversible oxygen redox chemistry in aqueous zinc-ion batteries, Angew. Chem. Int. Ed. 58 (2019) 7062–7067.

[103] G. Fang, S. Liang, Z. Chen, P. Cui, X. Zheng, A. Pan, B. Lu, X. Lu, J. Zhou, Simultaneous cationic and anionic redox reactions mechanism enabling high-rate long-life aqueous zinc-ion battery, Adv. Funct. Mater. 29 (2019) 1905267.

[104] L. Ma, N. Li, C. Long, B. Dong, D. Fang, Z. Liu, Y. Zhao, X. Li, J. Fan, S. Chen, S. Zhang, C. Zhi, Achieving both high voltage and high capacity in aqueous zinc-ion battery for record high energy density, Adv. Funct. Mater. 29 (2019) 1906142.

[105] P. Hu, M. Yan, T. Zhu, X. Wang, X. Wei, J. Li, L. Zhou, Z. Li, L. Chen, L. Mai, Zn/V_2O_5 aqueous hybrid-ion battery with high voltage platform and long cycle life, ACS Appl. Mater. Interfaces 9 (2017) 42717–42722.

[106] W. Zhang, S. Liang, G. Fang, Y. Yang, J. Zhou, Ultra-high mass-loading cathode for aqueous zinc-ion battery based on graphene-wrapped aluminum vanadate nanobelts, Nano-Micro Lett. 11 (2019) 69–80.

Update

Materials Today Advances

Volume 7, Issue , September 2020, Page

DOI: https://doi.org/10.1016/j.mtadv.2020.100093

Materials Today Advances 7 (2020) 100093

Contents lists available at ScienceDirect

Materials Today Advances

journal homepage: www.journals.elsevier.com/materials-today-advances/

Corrigendum to "Recent advances in cathode materials of rechargeable aqueous zinc ion batteries" [Mater. Today Adv. 7 (2020) 100078]

L. Wang, J. Zheng*

College of Chemistry and Molecular Engineering, Beijing National Laboratory for Molecular Sciences, Peking University, Beijing, 100871, China

The authors regret, In Table 2, the ref. [63] should be ref. [78].
The authors would like to apologise for any inconvenience caused.

DOI of original article: https://doi.org/10.1016/j.mtadv.2020.100078.
* Corresponding author.
E-mail address: junrong@pku.edu.cn (J. Zheng).

https://doi.org/10.1016/j.mtadv.2020.100093